Journal Pre-proofs

Modelling CO_2 absorption in aqueous solutions of cholinium lysinate ionic liquid

C.F. Martins, L.A. Neves, R. Chagas, L.M. Ferreira, C.A.M. Afonso, I.M. Coelhoso, J.G. Crespo, J.PB. Mota

PII: S1385-8947(20)33994-2
DOI: https://doi.org/10.1016/j.cej.2020.127875
Reference: CEJ 127875

To appear in: *Chemical Engineering Journal*

Received Date: 20 July 2020
Revised Date: 21 November 2020
Accepted Date: 23 November 2020

Please cite this article as: C.F. Martins, L.A. Neves, R. Chagas, L.M. Ferreira, C.A.M. Afonso, I.M. Coelhoso, J.G. Crespo, J.PB. Mota, Modelling CO_2 absorption in aqueous solutions of cholinium lysinate ionic liquid, *Chemical Engineering Journal* (2020), doi: https://doi.org/10.1016/j.cej.2020.127875

Modelling CO_2 absorption in aqueous solutions of cholinium lysinate ionic liquid

C. F. Martins,[a] L. A. Neves,[a] R. Chagas,[b] L. M. Ferreira,[a] C. A. M. Afonso,[c] I. M. Coelhoso,[a]

J. G. Crespo,[a,*] J. P. B. Mota[a,*]

[a] *LAQV/Requimte, Department of Chemistry, NOVA School of Science and Technology, NOVA University of Lisbon, 2829-516 Caparica, Portugal.*

[b] *i3N/CENIMAT Department of Materials Science, NOVA School of Science and Technology, NOVA University of Lisbon, 2829-516 Caparica, Portugal.*

[c] *Research Institute for Medicines (iMed.ULisboa), Faculty of Pharmacy, Universidade de Lisboa, Av. Prof. Gama Pinto, 1649-003 Lisbon, Portugal*

Abstract

Ionic liquids (ILs) with quaternary ammonium cations combined with biocompatible anions from renewable sources result in low-toxic, biocompatible, cost-efficient sorbent media that can efficiently capture carbon dioxide (CO_2). The understanding of the equilibrium and kinetics of CO_2 absorption in these media is relevant for the design of new absorption processes in many application areas, such as CO_2 removal from post-combustion streams, biogas refinery waste gases, or confined spaces. Here CO_2 absorption in an aqueous solution of cholinium lysinate IL is studied both theoretically, via mechanistic modelling, and experimentally in a membrane contactor operated in closed loop with online pH measurement and attenuated total reflectance Fourier transform infrared spectroscopy (ATR-FTIR) analysis of discrete sampling of the circulating aqueous IL solution. It is shown that both techniques are effective tools for CO_2 quantification in the liquid phase. The IL yields an absorption capacity of 2.20 moles of CO_2 per mole of IL for an IL concentration of 2.13 M (or 50 wt% solution). A comprehensive model of chemisorption thermodynamics and absorption dynamics is proposed and validated

experimentally. It provides not only the equilibrium constants of the reversible reactions of protonation of the amine groups and bicarbonate binding and overall mass-transfer coefficient based on liquid-phase concentrations, but is also the basis for a chemometric analysis of the experimental ATR-FTIR data. The potential use of ATR-FTIR as a monitoring tool of CO_2 in aqueous solutions of cholinium lysinate IL is also demonstrated.

Keywords: CO_2 capture, biocompatible ionic liquid, chemical model, Fourier-transform infrared spectroscopy.

1. Introduction

The development of new and more efficient carbon dioxide (CO_2) capture processes has been gaining the interest of both industry and academia over the years. According to the Scopus® database the main areas where CO_2 capture is more relevant are energy, engineering—especially chemical engineering — environmental and materials science, agricultural, and biological sciences. In medicine, CO_2 capture agents (e.g., soda lime) are essential for commercial application of inhaled anaesthetics, and thus, to the modern practice of anaesthesia [1].

There has been significant research on CO_2 capture and separation, but despite the emergence of new CO_2 capture agents, aqueous amine solutions (e.g., monoethanolamine and diethanolamine) are still the most commonly used absorbers [2,3]. There are, however, some niche applications where CO_2 cannot be captured using traditional aqueous amine solutions, such as hospital and medical clinic environments (e.g., surgical rooms), where the rules are extremely restrictive, especially regarding temperature, humidity, and cleaning conditions. The chemical degradation of aqueous amine solutions and vapour emissions that are produced during CO_2 capture hinder their use in hospital environments. Therefore, the selection and synthesis of a particular CO_2 capture agent depend on the type of application, and this has motivated researchers to seek alternatives to amine scrubbing [4,5].

Biocompatible amine-based agents possessing negligible volatility and excellent thermal stability, such as ionic liquids (ILs) with amine functionality, are desirable for the abovementioned niche applications, as is the case of medical environments. ILs with quaternary ammonium cations, of which the cholinium cation is a prominent example, are biocompatible and are much less toxic than most conventional room-temperature ILs (e.g., ILs with imidazolium cations). Moreover, unlike conventional ILs, those with quaternary ammonium cations are not limited to physical absorption since the amino groups can react with CO_2, allowing its chemisorption and thereby improving their CO_2 absorption capacity. The combination of the cholinium cation with biocompatible anions from renewable sources, such as amino acids, results in low toxic, biocompatible, and cost-effective ILs with recognised efficiency for CO_2 capture [6–10]. Furthermore, amino acid salts are known to have better oxidative stability than traditional aqueous amine solutions [11–13]. Fig. 1 shows the molecular structures of the cholinium cation and a generic amino acid anion, where R denotes an alkyl side chain with a functional group.

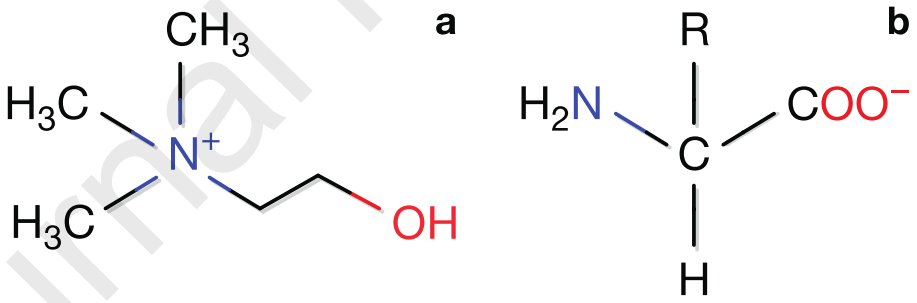

Figure 1. Molecular structures of (a) cholinium cation and (b) generic amino acid anion.

In addition to such desirable attributes as low environmental impact, high thermal and chemical stabilities, and fast absorption rate, the production cost of a new and efficient IL for CO_2 capture is also of great importance. For these reasons, cholinium-based ILs combined with amino acid anions are emerging as alternative absorption media for CO_2 capture. Additionally, the strategy of using aqueous solutions of functionalised ILs along with biocompatible and

biodegradable compounds is gaining projection in the CO_2 capture field, due to all the well-known environmental impact problems.

Many authors have investigated CO_2 absorption in IL solutions with increased content of functional amino groups with promising results [8,14–17]. Zhou *et al.* [15] developed a novel triamino-functionalized IL and measured its the CO_2 absorption capacity in a 0.5 M IL aqueous solution, reporting a very reasonable loading value of 1.59 moles of CO_2 per mole of IL. Yuan *et al.* [8] investigated CO_2 absorption in aqueous solutions with 5–30 wt% of three cholinium-based amino acid ILs. These authors observed an increase of the apparent absorption rate constant, a decrease of the solution viscosity, and reduction of the CO_2 absorption loading with the increase in water content. Additionally, the replacement of some of the IL by water reduces the cost of the aqueous IL solution. Therefore, to develop an efficient IL-based absorption medium competitive with current technologies, a trade-off must be found between the CO_2 loading and absorption rate.

Here we study CO_2 absorption in an aqueous solution with 50 wt% of cholinium lysinate ($[Cho^+][Lys^-]$) IL, where $[Cho^+]$ is the 2-hydroxy-N,N,N-trimethylethanaminium cation, commonly called cholinium cation, and $[Lys^-]$ the α-amino-acid anion ($C_6H_{13}N_2O_2^-$) that is the conjugate base of lysine, obtained from the deprotonation of the carboxyl group. The aqueous $[Cho^+][Lys^-]$ IL solution has an extremely high alkalinity (pH ~13). Cholinium is a quaternary ammonium cation, an essential micronutrient, which was chosen because of its recognized biocompatibility. Lysine is a basic amino acid that has two amino groups. In addition to the amino group of the carboxylic acid, the lysine's alkyl side chain contains another amino group that can also work as a base. Due to the high pKa values of the functional amino groups, lysine easily gains positive charge through proton binding at physiological pH. Because lysine can stablish acid-base Lewis interactions with CO_2 in aqueous media, allowing the capture of two molecules of CO_2 molecules per host molecule, it possesses favourable characteristics for CO_2 capture.

In addition to lysine, there are two other basic amino acids available, namely, histidine and arginine. Sistla and Khanna [14] combined several amino acid anions with the [bmim] cation

and tested them for CO_2 solubility. Of all the amino acid-ILs studied, [bmim][argininate] showed the highest CO_2 solubility (0.62 moles of CO_2 per mole of IL), followed by [bmim][lysinate] (0.48 moles of CO_2 per mole of IL), and [bmim][histidinate] (0.45 moles of CO_2 per mole of IL). Lysine and arginine are very similar in terms of toxicity, biodegradability, and cost [10]. However, the low water solubility of arginine is a serious limitation for CO_2 capture [18]. Dry cholinium-amino acid based ILs have high viscosities, which can only be overcome by combining them with water. Furthermore, the stronger interaction between CO_2 and arginine may invalidate the possibility of subsequent regeneration of the IL. For all of the mentioned reasons, lysine was the selected amino acid for the present study.

In our experimental setup for CO_2 absorption studies, the aqueous $[Cho^+][Lys^-]$ IL solution circulates in the lumen side of a polytetrafluoroethylene membrane contactor, while CO_2 circulates countercurrently, in closed-loop, in the shell side of the contactor. In a typical experimental run, the total amount of absorbed CO_2 is monitored in real-time up to the saturation conditions of the IL solution. The CO_2 concentration in the gas phase is monitored by gas chromatography and that in the aqueous IL solution by pH measurements and attenuated total reflectance Fourier-transform infrared spectroscopy (ATR-FTIR).

FTIR, along with nuclear magnetic resonance (NMR) and UV-vis spectroscopy (ultraviolet-visible), are techniques that can be used to obtain information about chemical equilibrium in solution. Besides being a non-destructive technique and requiring a small amount of sample, IR spectroscopy is much more reliable for the quantitative analysis of a compound that is physically or chemically similar to others in a mixture. Molecular differences between the structures of many chemical compounds can be identified and quantified in the mid-IR region between $4000–400\ cm^{-1}$ [19,20]. We have used this technique to analyze variations in the molecular structure and composition of the aqueous $[Cho^+][Lys^-]$ IL solution as a function of CO_2 loading.

The mechanisms by which CO_2 is absorbed in aqueous IL systems, where capture occurs by chemisorption, are not yet sufficiently understood. The study of the reactions involving (bi)carbonate and carbamate or carbamic acid formation is important for describing the reaction chemistry of CO_2 absorption in IL solutions. In this context, the present work reports a detailed modelling study of CO_2 absorption in aqueous $[Cho^+][Lys^-]$ IL solutions. To this end, a chemical model for the CO_2–H_2O–$[Cho^+][Lys^-]$ system is proposed and validated using the experimentally measured pH. Additionally, the use of ATR-FTIR and pH analysis as quantitative techniques for monitoring CO_2 absorption in the IL liquid solution is described. Our findings can be useful for other systems or processes, such as the removal of CO_2 from post-combustion streams, biogas refinery waste gases, or confined spaces (e.g. mines, spacecraft, and others).

2. Absorption model

The $[Lys^-]$ anion is an amphoteric compound that acts as a Lewis acid when combined with the $[Cho^+]$ cation due to the presence of the ammonium group in the latter. However, in the presence of water and CO_2 the $[Lys^-]$ anion acts as a base, leading to CO_2 chemisorption via a mechanism involving the direct formation of bicarbonate (HCO_3^-) and carbonate (CO_3^{2-}) and excluding the formation of carbamic acid [21,22]. There are reported evidences that carbamates can be formed with the carboxylic acid functional group of $[Lys^-]$, due to an intramolecular proton transfer from the α-ammonium ion to the carboxylate group [15,23]. Nevertheless, the carboxylic acid protonation occurs at acidic pH, where stable carbamates can be formed. However, the carboxylic acid group interacts with the cholinium cation through ionic coupling. Because of the high pH of the $[Cho^+][Lys^-]$ IL solution, the carbamate/carbonic acid formation mechanism is considered negligible in the present work. In aqueous media lysine is sensitive to pH and can assume four different ionisation states. Due to the presence of the three functional groups, there are three pK_a dissociation constants: their values for lysine are pK_{a1}= 2.15, pK_{a2}= 9.16, pK_{a3}= 10.67 [24], where pK_{a1} refers to the α-carboxylate group ($-COOH$), pK_{a2} to the α-ammonium ion ($-NH_3^+$),

and pK_{a3} to the $-NH_3^+$ side-chain group. Fig. 2 shows the different ionic states of lysine in aqueous solution.

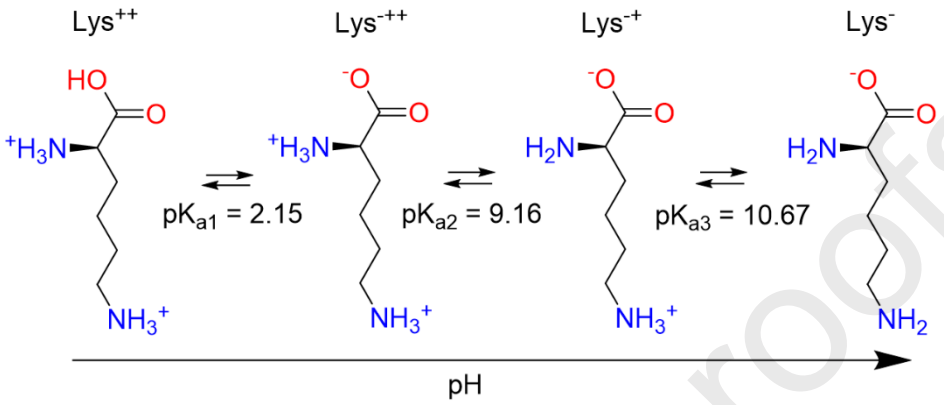

Figure 2. Dissociation states of lysine in aqueous solution.

Due to the formation of the bicarbonate in the presence of water, the interaction of CO_2 with the $[Cho^+][Lys^-]$ IL in aqueous solution is assumed to take place exclusively with the ionic forms of the lysinate anion. The bicarbonate anion can bind to the amine groups of lysine; thus, theoretically two molecules of CO_2 can be captured by one molecule of $[Cho^+][Lys^-]$ via chemisorption. The Lys^{++} ionic form is not present in our aqueous IL system, since Lys^{++} occurs only in acidic media, which is not the case here (the pH is always higher than ca. 8.0). Fig. 3 shows the possible forms of $[Cho^+][Lys^-]$ in aqueous solution during CO_2 absorption.

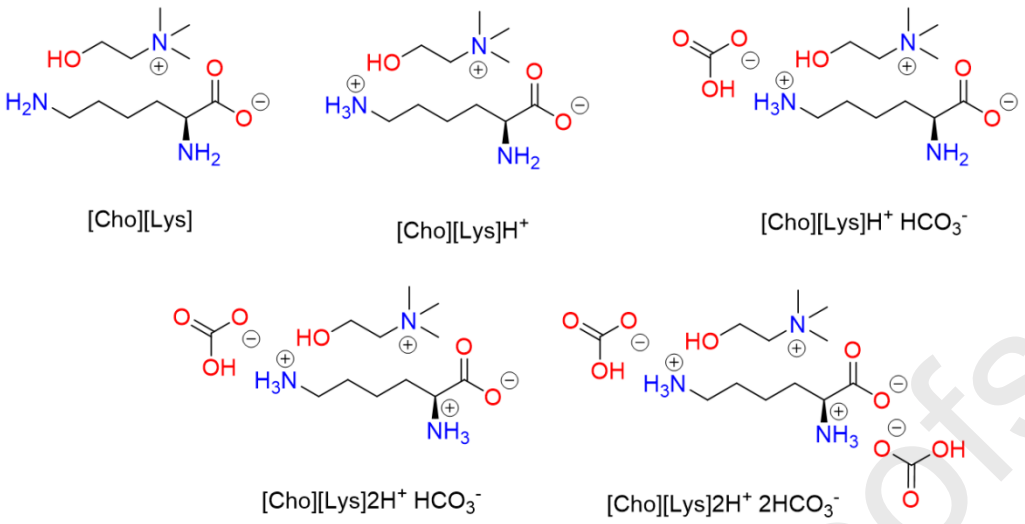

Figure 3. Structure of $[Cho^+][Lys^-]$ in water and in the presence of dissolved CO_2.

Based on these observations, we propose the reaction pathways pictured in Fig. 4 for the system CO_2–H_2O–$[Cho^+][Lys^-]$, which are supported by the hybrid quantum chemistry calculations based on density functional theory reported by Sun et al. [21]. It is assumed that all reaction pathways are reversible, but due to the fast conversion of the dissolved CO_2 into HCO_3^- and CO_3^{2-} in the aqueous IL medium (depending on the pH), its concentration is very low until near saturation conditions when it attains its solubility value. The set of governing reaction equations describing the proposed mechanism is

$$2H_2O \overset{K_1}{\leftrightarrow} H_3O^+ + OH^-, \quad (1)$$

$$CO_2 + 2H_2O \overset{K_2}{\leftrightarrow} HCO_3^- + H_3O^+, \quad (2)$$

$$HCO_3^- + H_2O \overset{K_3}{\leftrightarrow} CO_3^{2-} + H_3O^+, \quad (3)$$

$$R + H_3O^+ \overset{K_4}{\leftrightarrow} RH^+ + H_2O, \quad (4)$$

$$RH^+ + H_3O^+ \overset{K_5}{\leftrightarrow} RH_2^{2+} + H_2O, \quad (5)$$

$$RH^+ + HCO_3^- \overset{K_6}{\leftrightarrow} P_1, \quad (6)$$

$$P_1 + H_3O^+ \overset{K_7}{\leftrightarrow} P_1^+ + H_2O, \quad (7)$$

$$P_1^+ + HCO_3^- \overset{K_8}{\leftrightarrow} P_2, \quad (8)$$

where R denotes the $[Cho^+][Lys^-]$ IL, RH^+ and RH_2^{2+} the positively charged forms $[Cho^+][Lys^{-+}]$ and $[Cho^+][Lys^{-++}]$, $P_1 \equiv [Cho^+][Lys^{-+}HCO_3^-]$, $P_2 \equiv [Cho^+][Lys^{-++}2HCO_3^-]$ the final products, and $P_1^+ \equiv [Cho^+][Lys^{-++}HCO_3^-]$ an intermediate species.

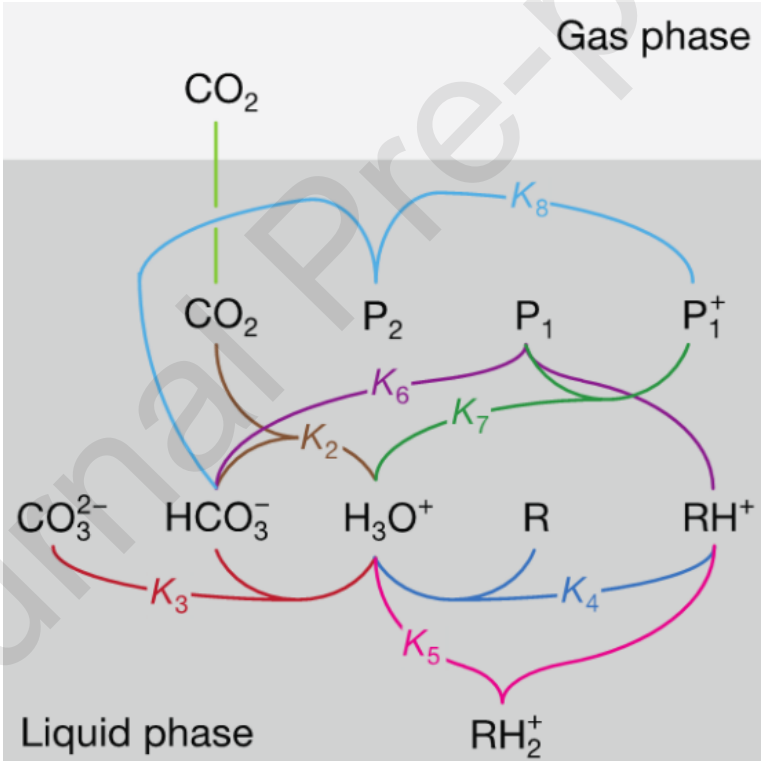

Figure 4. Proposed reaction pathways for the system CO_2–H_2O–$[Cho^+][Lys^-]$ (water dissociation reaction not included). R denotes the $[Cho^+][Lys^-]$ IL, RH^+ and RH_2^{2+} the positively charged forms $[Cho^+][Lys^{-+}]$ and $[Cho^+][Lys^{-++}]$, $P_1 \equiv [Cho^+][Lys^{-+}HCO_3^-]$, $P_2 \equiv [Cho^+][Lys^{-++}2HCO_3^-]$ the final products, and $P_1^+ \equiv [Cho^+][Lys^{-++}HCO_3^-]$ an intermediate species.

Additionally, if the CO_2 transfer rate to the liquid phase reactor is low enough, a quasi-equilibrium kinetic approximation can be invoked: the reactions are so much faster than the CO_2 transfer rate that they continuously equilibrate after a differential displacement from their previous equilibrium condition triggered by the small addition of CO_2. Thus, at each instant during and absorption experiment the concentrations of the various species in solution are governed by the corresponding chemical equilibrium constants. For each reaction, say

$$\sum_{i\epsilon\mathcal{R}} \nu_i R_i = \sum_{j\epsilon\mathcal{P}} \nu_j P_j, \tag{9}$$

where $\mathcal{R}$ is the set of reagents, $\mathcal{P}$ the set of products, and the ν's the stoichiometric coefficients. The corresponding equilibrium constant is defined as

$$K = \frac{\prod_{j\epsilon\mathcal{P}} (\gamma_j x_j)^{\nu_j}}{\prod_{i\epsilon\mathcal{R}} (\gamma_i x_i)^{\nu_i}}, \tag{10}$$

where x_i and γ_i are the mole fraction and activity coefficient of species i in solution.

If $\sum_{i\epsilon\mathcal{R}} \nu_i = \sum_{j\epsilon\mathcal{P}} \nu_j$, the mole fractions x_i and x_j can be replaced by the corresponding molar concentrations, $[R_i]$ and $[P_j]$, yielding

$$K = \frac{\prod_{j\epsilon\mathcal{P}} \gamma_j^{\nu_j}}{\prod_{i\epsilon\mathcal{R}} \gamma_i^{\nu_i}} \times \frac{\prod_{j\epsilon\mathcal{P}} [P_j]^{\nu_j}}{\prod_{i\epsilon\mathcal{R}} [R_i]^{\nu_i}}. \tag{11}$$

This happens in all cases except reactions (2), (6), and (8), whose equilibrium constants are expressed as

$$K_2 = \frac{(\gamma_{HCO_3^-})(\gamma_{H_3O^+})}{(\gamma_{CO_2})(\gamma_{H_2O})^2} \times \frac{[HCO_3^-][H_3O^+][S]}{[CO_2][H_2O]^2}, \tag{12}$$

$$K_6 = \frac{\gamma_{P_1}}{(\gamma_{RH^+})(\gamma_{HCO_3^-})} \times \frac{[P_1][S]}{[RH^+][HCO_3^-]}, \tag{13}$$

$$K_8 = \frac{\gamma_{P_2}}{(\gamma_{P_1})(\gamma_{HCO_3^-})} \times \frac{[P_2][S]}{[P_1][HCO_3^-]}, \tag{14}$$

where $[\mathrm{S}] = \sum_{i \in \mathcal{R}}[R_i] + \sum_{j \in \mathcal{P}}[P_j] = [\mathrm{H_2O}] + [\mathrm{OH^-}] + \cdots [\mathrm{P_2}]$ is the "total" molar concentration of the solution. The water equilibrium constant, K_1, and those for the $\mathrm{CO_2}$ dissociation, K_2 and K_3, were taken from the Aspen Plus library (ver. 10.2) and are listed in Table 1. The unknown equilibrium constants are K_4, K_5, K_6, K_7 and K_8.

Table 1. Equilibrium constants for the absorption reactions of $\mathrm{CO_2}$ in water.

Equilibrium constant	Value
K_1	2.208×10^{-18}
K_2	7.350×10^{-9}
K_3	7.499×10^{-13}

The liquid-phase properties and activity coefficients are estimated using the unsymmetrical electrolyte NRTL property method (eNRTL) [25–27] and the gas-phase properties with the Redlich-Kwong equation of state [28] as implemented in Aspen Plus (ver. 10.2).

Although $[\mathrm{Cho^+}][\mathrm{Lys^-}]$, $[\mathrm{Cho^+}][\mathrm{Lys^{-+}}]$, $[\mathrm{Cho^+}][\mathrm{Lys^{-++}}]$, $[\mathrm{Cho^+}][\mathrm{Lys^{-+}HCO_3^-}]$, and $[\mathrm{Cho^+}][\mathrm{Lys^{-++}2HCO_3^-}]$ are not in the Aspen Plus database, we proceed as follows. Because the logarithm of the activity coefficient can be split into the sum of a term accounting to local interactions that exist at the immediate neighbourhood of any species and the other from the long-range ion–ion interactions that exist beyond the immediate vicinty of an ionic species, and each segment of a molecule contributes nearly additively to those two terms, the ratios of activity coefficients for the equilibrium constants involving the IL or its derivatives can be simplified as follows:

$$\frac{(\gamma_{\mathrm{RH^+}})(\gamma_{\mathrm{H_2O}})}{(\gamma_{\mathrm{R}})(\gamma_{\mathrm{H_3O^+}})} \approx \frac{(\gamma_{\mathrm{Lys-+}})(\gamma_{\mathrm{H_2O}})}{(\gamma_{\mathrm{Lys-}})(\gamma_{\mathrm{H_3O^+}})}, \tag{15}$$

$$\frac{(\gamma_{\mathrm{RH_2^+}})(\gamma_{\mathrm{H_2O}})}{(\gamma_{\mathrm{RH}^+})(\gamma_{\mathrm{H_3O}^+})} \approx \frac{(\gamma_{\mathrm{Lys}^{\mp}+})(\gamma_{\mathrm{H_2O}})}{(\gamma_{\mathrm{Lys}^{\mp}})(\gamma_{\mathrm{H_3O}^+})}, \tag{16}$$

$$\frac{\gamma_{\mathrm{P_1}}}{(\gamma_{\mathrm{RH}^+})(\gamma_{\mathrm{HCO_3^-}})} \approx \frac{\gamma_{\mathrm{Lys}^{-+}}}{(\gamma_{\mathrm{Lys}^{\mp}+})(\gamma_{\mathrm{HCO_3^-}})}, \tag{17}$$

$$\frac{(\gamma_{\mathrm{P_1^+}})(\gamma_{\mathrm{H_2O}})}{(\gamma_{\mathrm{P_1}})(\gamma_{\mathrm{H_3O}^+})} \approx \frac{(\gamma_{\mathrm{Lys}^{\mp}+})(\gamma_{\mathrm{H_2O}})}{(\gamma_{\mathrm{Lys}^{\mp}})(\gamma_{\mathrm{H_3O}^+})}, \tag{18}$$

$$\frac{\gamma_{\mathrm{P_2}}}{(\gamma_{\mathrm{P_1}})(\gamma_{\mathrm{HCO_3^-}})} \approx \frac{(\gamma_{\mathrm{Lys}^{\mp}+})(\gamma_{\mathrm{HCO_3^-}})}{\gamma_{\mathrm{Lys}^{-+}}}, \tag{19}$$

These equations involve the ratios $(\gamma_{\mathrm{Lys}^{-+}})/(\gamma_{\mathrm{Lys}^{-}})$ and $(\gamma_{\mathrm{Lys}^{-++}})/(\gamma_{\mathrm{Lys}^{-+}})$, which in both cases correspond to the protonation of an amine group, $-\mathrm{NH_2} \Longrightarrow -\mathrm{NH_3^+}$. Using the unsymmetrical Pitzer–Debye–Huckel formula [29] (on which the eNRTL model rests) to account for the long-range (electrostatic) interactions, each of these $\gamma's$ can be approximated as

$$\ln \gamma_i = -\left(\frac{1000}{M_s}\right)^{1/2} A_\varphi \left[\left(\frac{2z_i^2}{\rho}\right)\ln\left(1+\rho I_x^{1/2}\right) + \frac{z_i^2 I_x^{1/2} - 2I_x^{1/2}}{1+\rho I_x^{1/2}}\right]. \tag{20}$$

Here, $I_x = \frac{1}{2}\sum z_j^2 x_j$ is the ionic strength of the aqueous IL solution on a mole fraction basis, where z_j and x_j are the charge number and mole fraction of ionic segment j ($\mathrm{H_3O^+}$, $\mathrm{OH^-}$, $\mathrm{HCO_3^-}$, $\mathrm{CO_3^{2-}}$, $-\mathrm{O^-}$, and $-\mathrm{NH_3^+}$), ρ the closest approach parameter, A_φ the Debye-Hckel parameter, and M_s the molecular weight of the solvent [29]. Applying eq. (20) to the ratio of two γ's, say γ_b/γ_a, gives

$$\ln\frac{\gamma_b}{\gamma_a} = -\left(\frac{1000}{M_s}\right)^{1/2} A_\varphi \left[\frac{2}{\rho}\ln\left(1+\rho I_x^{1/2}\right) + \frac{I_x^{1/2}}{1+\rho I_x^{1/2}}\right]\left(z_b^2 - z_a^2\right). \tag{21}$$

In Aspen Plus we use n-dimethylethanolamine ($\mathrm{C_4H_{12}NO^+}$) as a surrogate for $\mathrm{Cho^+}$ and octanoate ($\mathrm{C_7H_{15}COO^-}$) for $\mathrm{Lys^-}$; these components are the ones with characteristics closest to the IL's cation and anion that could be found in the database.

Since a quasi-equilibrium kinetic approximation is used for the absorption model, it is convenient to introduce the extent of reaction, ξ, a quantity that measures the extent at which a reaction proceeds [30], for it makes it easier to write down the differential material balances.

Let ξ_n be the extent of reaction n. The differential material for each species in the system, say the i^{th} one, S_i, can then be written in terms of its molar concentration, $[S_i]$, and the extents of the reactions in which it participates either as a reagent or product. Applying this procedure to all species in the system gives rise to the following differential material balances:

$$d[\mathrm{H_2O}] = -2d\xi_1 - 2d\xi_2 - d\xi_3 + d\xi_4 + d\xi_5 + d\xi_7, \tag{22}$$

$$d[\mathrm{H_3O^+}] = d\xi_1 + d\xi_2 + d\xi_3 - d\xi_4 - d\xi_5 - d\xi_7, \tag{23}$$

$$d[\mathrm{OH^-}] = d\xi_1, \tag{24}$$

$$d[\mathrm{HCO_3^-}] = d\xi_2 - d\xi_3 - d\xi_6 - d\xi_8, \tag{25}$$

$$d[\mathrm{CO_3^{2-}}] = d\xi_3, \tag{26}$$

$$d[\mathrm{R}] = -d\xi_4, \tag{27}$$

$$d[\mathrm{RH^+}] = d\xi_4 - d\xi_5 - d\xi_6, \tag{28}$$

$$d[\mathrm{RH_2^{2+}}] = d\xi_5, \tag{29}$$

$$d[\mathrm{P_1}] = d\xi_6 - d\xi_7, \tag{30}$$

$$d[\mathrm{P_1^+}] = d\xi_7 - d\xi_8, \tag{31}$$

$$d[\mathrm{P_2}] = d\xi_8. \tag{32}$$

Note that no differential material balance is written for $[\mathrm{CO_2}]$ (dissolved carbon under $\mathrm{CO_2}$ form); instead, the material balances are subjected to the additional condition

$$[\mathrm{CO_2}] + [\mathrm{HCO_3^-}] + [\mathrm{CO_3^{2-}}] + [\mathrm{P_1}] + [\mathrm{P_1^+}] + 2[\mathrm{P_2}] = [\mathrm{C_{tot}}], \tag{33}$$

where $[C_{tot}]$ is the total concentration of CO_2-derived species in the reaction medium at each instant. $[C_{tot}]$ is obtained from the differential material balance to the CO_2 fed to the system:

$$\frac{d[VC_{tot}]}{dt} = \Delta\dot{n}_{CO_2}, \quad \Delta\dot{n}_{CO_2} \equiv \dot{n}_{CO_2}^{(in)} - \dot{n}_{CO_2}^{(out)}, \qquad \text{s.t. } [C_{tot}]_{t=0} = 0, \tag{34}$$

or in integrated form,

$$[C_{tot}](t) = \frac{1}{V}\int_0^t \Delta\dot{n}_{CO_2} dt, \tag{35}$$

where V is the volume of the reaction medium in the membrane contactor (which remains practically constant over the course of the absorption experiment) and $\dot{n}_{CO_2}^{(in)}$ and $\dot{n}_{CO_2}^{(out)}$ the inlet and outlet molar flowrates of CO_2 in the shell side of the membrane contactor.

The initial conditions of the experiment are those before the injection of CO_2 when the amount of dissolved CO_2 is negligible, which in turn implies that the only species in solution are H_2O, OH^-, H_3O^+, R, RH^+ and RH_2^{2+}, and $[CO_2]_0 = [HCO_3^-]_0 = [CO_3^{2-}]_0 = [P_1]_0 = [P_1^+]_0 = [P_2]_0 = 0$. Taking this into account, the integration of the differential equations yields

$$[H_2O] = [H_2O]_0 - 2\xi_1 - 2\xi_2 - \xi_3 + \xi_4 + \xi_5 + \xi_7, \tag{36}$$

$$[H_3O^+] = [H_3O^+]_0 + \xi_1 + \xi_2 + \xi_3 - \xi_4 - \xi_5 - \xi_7, \tag{37}$$

$$[OH^-] = [OH^-]_0 + \xi_1, \tag{38}$$

$$[HCO_3^-] = \xi_2 - \xi_3 - \xi_6 - \xi_8, \tag{39}$$

$$[CO_3^{2-}] = \xi_3, \tag{40}$$

$$[R] = [R]_0 - \xi_4, \tag{41}$$

$$[RH^+] = [RH^+]_0 + \xi_4 - \xi_5 - \xi_6, \tag{42}$$

$$[RH_2^{2+}] = [RH_2^{2+}]_0 + \xi_5, \tag{43}$$

$$[P_1] = \xi_6 - \xi_7, \tag{44}$$

$$[P_1^+] = \xi_7 - \xi_8, \quad (45)$$

$$[P_2] = \xi_8, \quad (46)$$

$$[CO_2] = [C_{tot}] - [HCO_3^-] - [CO_3^{2-}] - [P_1] - [P_1^+] - 2[P_2], \quad (47)$$

where $[H_2O]_0$, $[OH^-]_0$, $[H_3O^+]_0$, $[R]_0$, $[RH^+]_0$, $[RH_2^{2+}]_0$ are the initial concentrations of the various species in solution. The initial conditions for the extents of reaction are simply $(\xi_n)_{t=0} = 0\ \forall n$. Although these equations can be solved as a function of reaction time, it is best to solve them for increasing values of $[C_{tot}]$; that is, to use $[C_{tot}]$ as the independent variable instead of time because the system is assumed to be equilibrium driven, as mentioned before. In this case the equations are

$$[H_2O]' = (-2\xi_1 - 2\xi_2 - \xi_3 + \xi_4 + \xi_5 + \xi_7)', \quad [H_2O]_{t=0} = [H_2O]_0, \quad (48)$$

$$[H_3O^+]' = (\xi_1 + \xi_2 + \xi_3 - \xi_4 - \xi_5 - \xi_7)', \quad [H_3O^+]_{t=0} = [H_3O^+]_0, \quad (49)$$

$$[OH^-]' = (\xi_1)', \quad [OH^-]_{t=0} = [OH^-]_0, \quad (50)$$

$$[HCO_3^-]' = (\xi_2 - \xi_3 - \xi_6 - \xi_8)', \quad [HCO_3^-]_{t=0} = 0, \quad (51)$$

$$[CO_3^{2-}]' = (\xi_3)', \quad [CO_3^{2-}]_{t=0} = 0, \quad (52)$$

$$[R]' = (-\xi_4)', \quad [R]_{t=0} = [R]_0, \quad (53)$$

$$[RH^+]' = (\xi_4 - \xi_5 - \xi_6)', \quad [RH^+]_{t=0} = [RH^+]_0, \quad (54)$$

$$[RH_2^{2+}]' = (\xi_5)', \quad [RH_2^{2+}]_{t=0} = 0, \quad (55)$$

$$[P_1]' = (\xi_6 - \xi_7)', \quad [P_1]_{t=0} = 0, \quad (56)$$

$$[\mathrm{P_1^+}]' = (\xi_7 - \xi_8)', \qquad [\mathrm{P_1^+}]_{t=0} = 0, \tag{57}$$

$$[\mathrm{P_2}]' = (\xi_8)', \qquad [\mathrm{P_2}]_{t=0} = 0, \tag{58}$$

where $[\mathrm{H_2O}]'$ is a shorthand notation for $d[\mathrm{H_2O}]/d[\mathrm{C_{tot}}]$, $(\xi_n)'$ for $d\xi_n/d[\mathrm{C_{tot}}]$, and so forth. These equations are further subjected to the condition given by equation (47).

3. Experimental

$[\mathrm{Cho^+}][\mathrm{Lys^-}]$ ionic liquid was synthesised from choline hydroxide solution (45 wt% aqueous solution, Acros Organics, USA) and L(+)-Lysine monohydrate (99%, Acros Organics, USA), supplied by Thermofisher Scientific. The $\mathrm{CO_2}$ used in the experiments was high-purity grade (99.998%) from Praxair, USA.

$\mathrm{CO_2}$ was captured from the gas phase into the aqueous IL solution flowing in a membrane contactor countercurrently to the gas phase, as represented in Figure 5. The membrane module consists of a set of Eclipse™ capillary membranes, supplied by Markel Corporation (USA), and made of microporous polytetrafluoroethylene, assembled in a stainless-steel housing. Since the focus of the present work is the theoretical study of $\mathrm{CO_2}$ capture by the aqueous IL solution, with emphasis on the chemical equilibrium behind the absorption process, the setup is not described in much detail here; a comprehensive description can be found elsewhere [31].

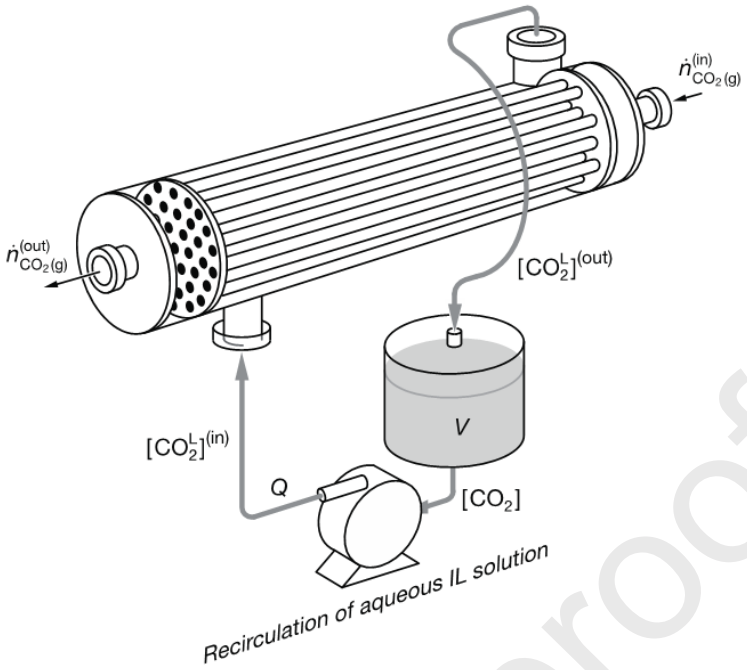

Figure 5. Schematic of the experimental set-up. The IL solution circulates in the lumen side of a polytetrafluoroethylene membrane contactor, while CO_2 circulates countercurrently in the shell side of the contactor. The system is operated in closed loop. $\dot{n}^{(in)}_{CO_2(g)}$ and $\dot{n}^{(out)}_{CO_2(g)}$ are the inlet and outlet molar flowrates of gaseous CO_2 in the lumen side of the contactor; $[CO_2^L]^{(in)}$ and $[CO_2^L]^{(out)}$ the inlet and outlet concentrations of aqueous CO_2 in the lumen (L) side of the membrane; V the volume of aqueous IL solution and Q the volumetric recirculation flow rate in the lumen side of the membrane. By definition $[CO_2^L]^{(in)} = [CO_2]$, where $[CO_2]$ is the concentration of dissolved CO_2 (i.e. CO_2, HCO_3^- and CO_3^{2-}) in the bulk of the aqueous IL solution, because the volume V is assumed to be perfectly mixed.

The CO_2 absorption reaction was followed by pH measurement, using a Mettler Toledo pH probe (model l405-DPAS-SC-K8S, USA) connected to an in-line tester (Jenco, model 3621, USA). ATR-FTIR analysis was used as well to monitor the absorption reaction off-line, using a Perkin Elmer Spectrum Two FT-IR Spectrometer at room temperature. Small samples (5×10^{-5} moles) of the liquid phase were collected periodically at a sampling rate of 3 min and later analysed by ATR-FTIR. The molecular structure of the synthesised $[Cho^+][Lys^-]$ IL was confirmed by proton nuclear magnetic resonance (^{1}H-NMR) on a Bruker AVANCE Digital

operating at 400 MHz. The water content of the IL solution was measured by titration, using a Karl-Fischer coulometer without diaphragm (Metrohm, USA, model 831 KF coulometer).

4. Results and discussion

4.1. Infrared characterisation of aqueous [Cho⁺][Lys⁻] solution

To monitor CO_2 absorption into aqueous $[\mathrm{Cho}^+][\mathrm{Lys}^-]$ IL solution with ATR-FTIR spectroscopy, a prior understanding of $[\mathrm{Cho}^+][\mathrm{Lys}^-]$ forms in the aqueous system is needed. ATR-FTIR spectra were obtained between $4000\text{–}400\ \mathrm{cm}^{-1}$ because the molecular deformations are detectable in the mid-IR region. Over this IR range, it is possible to identify and quantify the various species and functional groups relevant to the CO_2–water–$[\mathrm{Cho}^+][\mathrm{Lys}^-]$ system.

The IR spectra were obtained under different water activity (a_w) conditions, which correspond to different cholinium lysinate concentrations; $a_\mathrm{w} = \gamma_\mathrm{w} x_\mathrm{w}$, where γ_w is the activity coefficient of water and x_w the mole fraction of water in the aqueous fraction [7]. Changing a_w alters the water content of the cholinium lysinate IL and consequently the pH of the medium. As mentioned in Section 2, the lysinate anion assumes different protonated forms in the amine sites according to the pH. Fig. 6 shows the spectra of four different aqueous $[\mathrm{Cho}^+][\mathrm{Lys}^-]$ IL solutions for which representative differences were obtained over the range $1700\text{–}1200\ \mathrm{cm}^{-1}$ of wavenumbers. The main differences are characterised by deviations of the absorbance bands intensities at $1647\ \mathrm{cm}^{-1}$, $1558\ \mathrm{cm}^{-1}$, $1478\ \mathrm{cm}^{-1}$, $1408\ \mathrm{cm}^{-1}$, and $1358\ \mathrm{cm}^{-1}$. A very broad band between $3700\text{–}3000\ \mathrm{cm}^{-1}$ was also obtained, but it which is not shown here because it corresponds to the O–H stretching of water.

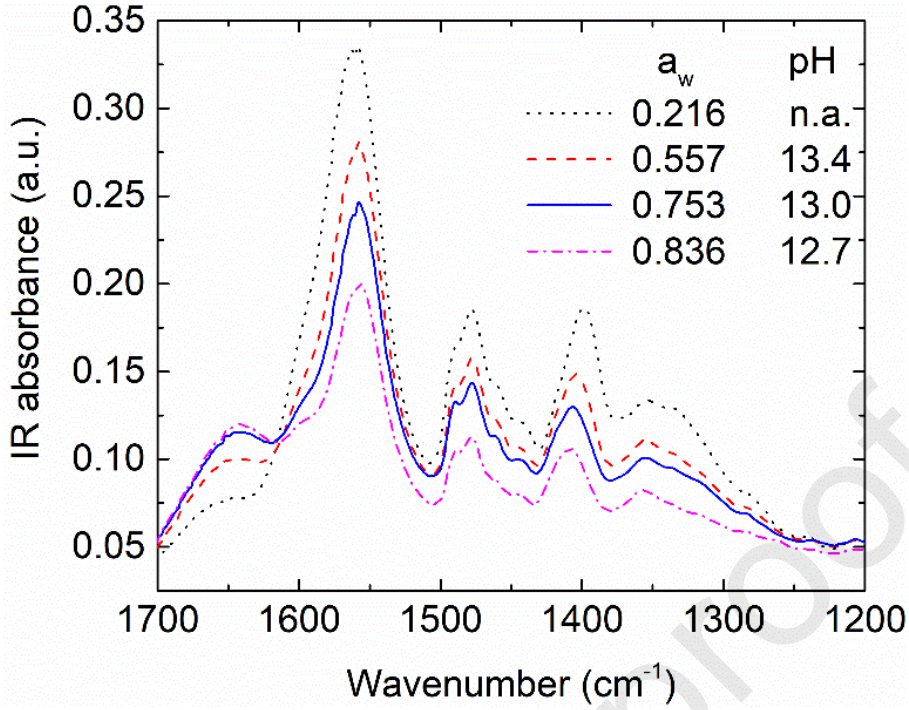

Figure 6. FTIR spectra of four $[\mathrm{Cho}^+][\mathrm{Lys}^-]$ IL solutions equilibrated at different values of water activity, a_w.

With the exception of the absorbance band at 1647 cm^{-1}, all the others increase as a_w decreases for more concentrated samples. The absorbance band ascribed to the $-\mathrm{NH}_3^+$ group is usually observed in the region 1750–1600 cm^{-1} [14]. Therefore, the band at 1647 cm^{-1} is attributed to the protonated amino groups, whose formation in the Lys anion is expected with the decrease of the pH, as demonstrated in Section 2 and shown in Fig. 6. Depending on the molecular constituents, carboxylate bands are generally present in the 1650–1540 cm^{-1} and 1450–1360 cm^{-1} regions. Therefore, the bands at 1558 cm^{-1} and 1408 cm^{-1} correspond to asymmetric and symmetric stretching vibrations of the C=O bond, respectively, which are present in the acidic group of the lysinate anion. Finally, the bands at 1478 cm^{-1} and 1358 cm^{-1} are associated with the C–H stretching vibrations of the methyl groups ($-\mathrm{CH}_3$) [20,32].

4.2. CO_2 absorption monitoring

The absorption kinetics of CO_2 into an aqueous solution containing 50 wt% of $[Cho^+][Lys^-]$ was measured at 22 °C (±2 °C) up to the conditions corresponding to the complete saturation. The transport of CO_2 in this solution is dominantly controlled by the chemical reaction equilibria, despite physical diffusion being present. Due to the strong basicity, the IL solution is very reactive towards CO_2 which behaves as Lewis acid. Therefore, CO_2 chemisorption in the present system occurs as a neutralisation reaction accompanied by a decrease in pH. In fact, the pH measurement throughout the whole absorption process proved to be quite useful for model validation, as will be demonstrated further ahead. Fig. 7 shows the experimentally measured pH as a function of reaction time, as well as the total amount of CO_2 absorbed by the aqueous IL solution, the latter computed from a material balance to the gas phase, eq. (34), from the measured values of $\Delta\dot{n}_{CO_2}$. The aqueous IL solution was completely saturated with CO_2 at pH ~ 8; under these conditions the CO_2 capture capacity was found to be ~ 2.2 mol CO_2/mol IL.

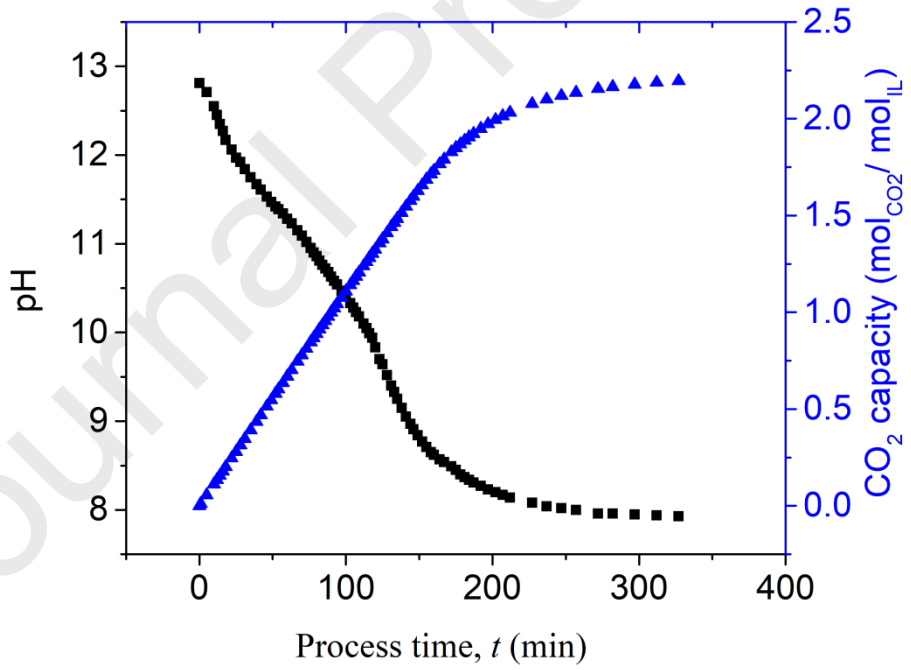

Figure 7. pH and total CO_2 solubility in the aqueous solution of 50 wt% $[Cho^+][Lys^-]$ as function of process time at 22 °C.

The strong basicity of the IL solution is confirmed by the initial pH shown in Fig. 7 (pH ~ 13). At this pH the amine of the alkyl side chain of Lys anion can be partially protonated since the corresponding pK_a is 10.67; consequently, the CO_2 molecules converted into HCO_3^- ions bind first to this amine. As CO_2 is progressively absorbed and the pH decreases towards its pK_a value of ca. 9.16, the amine of the carboxylic acid functional group will be able to protonate and bind to the bicarbonate ion.

As mentioned before, theoretically two molecules of CO_2 can react with one molecule of $[Cho^+][Lys^-]$, because CO_2 in the bicarbonate ion form can bind to both amines of the lysinate anion. From the results shown in Fig. 7, half of the total CO_2 capacity of the 50 wt% of $[Cho^+][Lys^-]$ IL solution (~ 1 mol CO_2/mol IL) is attained near $pK_{a3} = 10.67$, which means that around 50% of the amines of the lysinate anion are in solution, and in particular those of the alkyl side chain, established a bond with the bicarbonate ions. As these amines are being "occupied" and CO_2 continues to be absorbed, the α-amine of the carboxylic acid functional group starts to receive the bicarbonate ions as a second absorption wave, until the saturation state of the IL solution is reached. The complete saturation state was confirmed by the experimentally measured CO_2 capacity, which was determined using eq. (34) from the moment the outlet molar flow rate, $\dot{n}_{CO_2}^{(out)}$, attained and stabilised at the inlet value, $\dot{n}_{CO_2}^{(in)}$.

In addition to pH measurements, samples of the aqueous IL solution were periodically collected during the CO_2 absorption experiment and later analysed by ATR-FTIR. Fig. 8 shows the IR spectra of the aqueous IL solution with different CO_2 loadings. The observed variations in the spectrum are correlated with the different CO_2 loadings. The IR absorbance increases as more CO_2 is captured, which is a consequence of the increasing number of absorbing species in the aqueous $[Cho^+][Lys^-]$ IL solution. It is possible to assign IR absorbance bands to different characteristic species for the interactions between CO_2 and $[Cho^+][Lys^-]$. It is challenging to unambiguously assign all the absorbance bands because of band overlapping due to the coexistence of many absorbing species in solution. Nevertheless, the absorbance bands at 1647

cm^{-1}, 1478 cm^{-1}, and 1358 cm^{-1} were selected as the less prone to uncertainty and assigned to $-NH_3^+$, CO_3^{2-} and HCO_3^-, respectively.

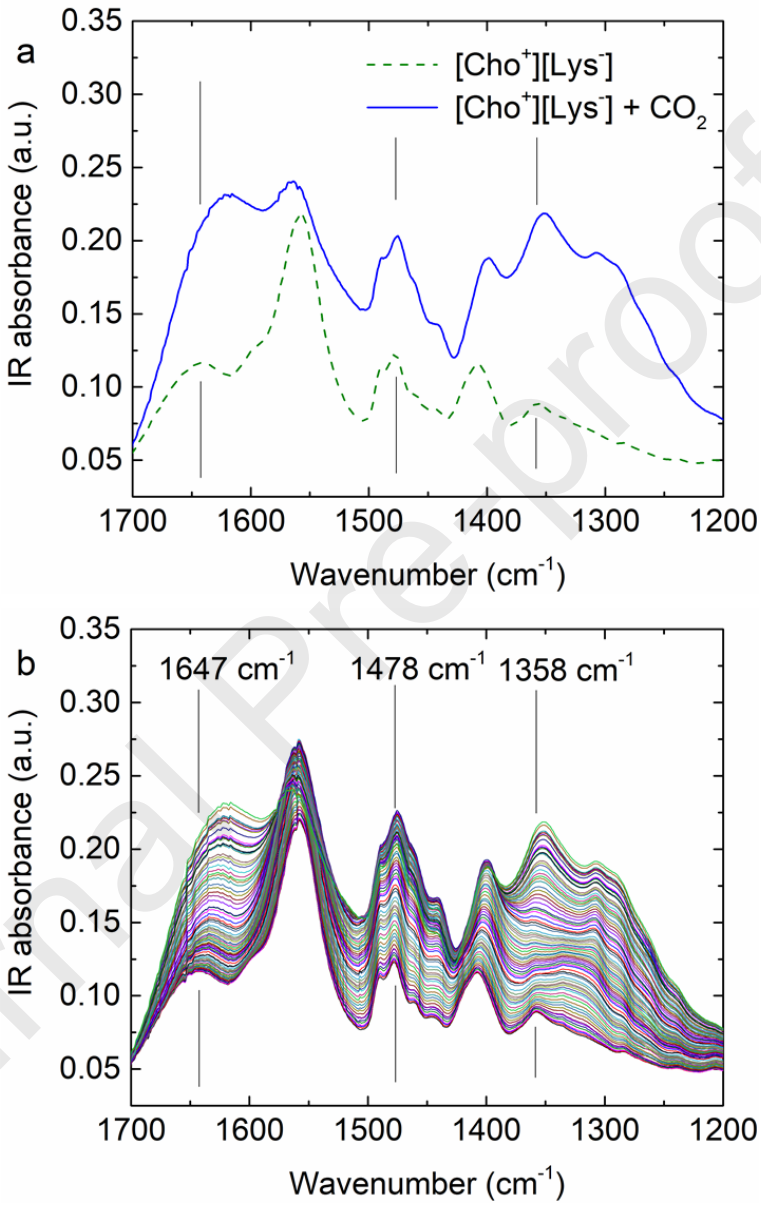

Figure 8. ATR-FTIR spectra. (a) Before and after CO_2 absorption into aqueous solution of 50 wt% [Cho^+][Lys^-] IL. (b) Aqueous solution of 50 wt% [Cho^+][Lys^-] IL with different CO_2 loadings.

As mentioned in Section 4.1., the absorbance band assigned to $-NH_3^+$ is usually located in the 1750–1600 cm^{-1} region; therefore, changes in the peak at 1647 cm^{-1} are assumed to

correlate with the protonation of the amines of the lysinate anion. Since the order of the C–O bond of the inorganic carbonates is between one and two, it exhibits a stretching vibration band in the $1510–1410\ \mathrm{cm}^{-1}$ region; thus, the identified band at $1478\ \mathrm{cm}^{-1}$ is attributed to the vibration of the carbonate ion, CO_3^{2-}. Finally, during the absorption CO_2 is converted into bicarbonate ion, whose formation is observed with the increase of the absorbance band at $1358\ \mathrm{cm}^{-1}$, as reported elsewhere [20,33].

The most commonly proposed reaction mechanism for CO_2 capture in traditional aqueous amine solutions with high water content considers the path carbamate → bicarbonate → carbonate formation [23]. This pathway considers amine to be the primary nucleophile for an attack on CO_2. Nevertheless, it has been reported that amino acid anions like $[Lys^-]$can take an alternative path. The proposed mechanism in this study considers the direct formation of bicarbonate where the first step is the amine protonation, which is confirmed by the results obtained. On the other hand, the carbamate/carbamic acid formation is excluded from the proposed chemical mechanism because no changes in the absorbance band in the $3000–2500\ \mathrm{cm}^{-1}$ region were observed.

4.3. Model fitting and validation

The chemical reactions governing CO_2 absorption in the aqueous $[Cho^+][Lys^-]$ IL solution are assumed to be given by the set of eqs. (1–8). The equilibrium constants K_1, K_2 and K_3, which characterise the water equilibrium and reversible reactions for CO_2 dissociation in aqueous solution were taken from the Aspen Plus (ver. 10.2) library and not subjected to any data fitting. The other equilibrium constants, namely K_4, K_5, and K_7 which characterise the reversible reactions of amine protonation of the lysinate anion, and K_6 and K_8, governing the bicarbonate ion binding, were fitted to the experimental pH and IR absorbance data.

The initial absorption medium consisted of 700 mL of an aqueous solution with 1.49 moles of IL dissolved into 21.18 moles of water, where $[R]_0 = 2.12$ M and $[H_2O]_0 = 30.26$ M.

The initial pH was 12.88. Hence, the model described in Section 2 should satisfy the following initial conditions:

$$[H_2O]_0 = 30.26\ \text{M}, \tag{59}$$

$$pH_0 = 12.88, \tag{60}$$

$$[R]_0 + [RH^+]_0 + [RH_2^{2+}]_0 = 2.12\ \text{M}, \tag{61}$$

$$[CO_2]_0 = [HCO_3^-]_0 = [CO_3^{2-}]_0 = [P_1]_0 = [P_1^+]_0 = [P_2]_0 = 0. \tag{62}$$

The CO_2 solubility in the aqueous solution of $[Cho^+][Lys^-]$, at 1 atm and 20 °C, is estimated to be $[CO_2]_{max} = 0.019$ M; this value was determined in Aspen Plus (ver. 10.2) using the unsymmetrical electrolyte NRTL property method (eNRTL-RK) and Redlich-Kwong equation of state for the gas phase. At the end of the experiment, the solution is known to be fully saturated because by then the inlet and outlet molar flowrates of gaseous CO_2 are identical. The measured pH under saturation conditions was 7.93. Moreover, by applying eq. (35) to the experimental data, the total amount of absorbed CO_2 under saturation conditions was found to be 3.13 M. Under these saturation conditions the concentration of aqueous CO_2 should be 0.019 M. Thus, the model should satisfy the following conditions at the end ($t \to \infty$) of the simulated experiment: $[CO_2]_\infty = 0.019$ M, $pH_\infty = 7.93$ and $[C_{tot}]_\infty = 3.13$ M. It is instructive to analyse the degrees of freedom of the problem. The equations governing the initial conditions of the experiment are[1]

$$[CO_2]_0 = [HCO_3^-]_0 = [CO_3^{2-}]_0 = [P_1]_0 = [P_1^+]_0 = [P_2]_0 = 0, \tag{63}$$

$$[H_2O]_0 = 30.26\ \text{M}, \tag{64}$$

$$pH_0 = 12.88, \tag{65}$$

[1]For simplicity the activity coefficients have been omitted from these equations but considered in the actual model.

$$[\mathrm{R}]_0 + [\mathrm{RH}^+]_0 + [\mathrm{RH}_2^{2+}]_0 = 2.13\ \mathrm{M}, \tag{66}$$

$$[\mathrm{H_3O}^+]_0 + [\mathrm{RH}^+]_0 + 2[\mathrm{RH}_2^{2+}]_0 = [\mathrm{OH}^-]_0, \tag{67}$$

$$\frac{[\mathrm{H_3O}^+]_0[\mathrm{OH}^-]_0}{([\mathrm{H_2O}]_0)^2} = K_1\,, \tag{68}$$

$$\frac{[\mathrm{RH}^+]_0[\mathrm{H_2O}]_0}{[\mathrm{R}]_0[\mathrm{H_3O}^+]_0} = K_4\,, \tag{69}$$

$$\frac{[\mathrm{RH}_2^{2+}]_0[\mathrm{H_2O}]_0}{[\mathrm{RH}^+]_0[\mathrm{H_3O}^+]_0} = K_5\,. \tag{70}$$

This set of equations has one degree of freedom: it has five unknown variables—$[\mathrm{R}]_0$, $[\mathrm{RH}^+]_0$, $[\mathrm{RH}_2^{2+}]_0$, K_4 and K_5—and four equations—(66), (67), (69), and (70). Hence, if say the ratio of equilibrium constants

$$\frac{K_5}{K_4} = \frac{[\mathrm{RH}_2^{2+}]_0[\mathrm{R}]_0}{([\mathrm{RH}^+]_0)^2} \tag{71}$$

are known, $[\mathrm{R}]_0$, $[\mathrm{RH}^+]_0$, $[\mathrm{RH}_2^{2+}]_0$, K_4, and K_5 can be determined from the initial conditions of the experiment.

The final conditions of the experiment reduce the number of degrees of freedom by two, because the values of pH_∞ and $[\mathrm{CO_2}]_\infty$ are known. This means that the three equilibrium constants K_6, K_7, and K_8 can be determined if the value of one of them is known. To summarise, the model has two degrees of freedom: e.g., the ratio K_5/K_4 and K_6.

The unknown equilibrium constants were determined by nonlinear least squares fitting of the experimental pH curve as a function of $[\mathrm{C_{tot}}]$. That is, the optimisation problem

$$\min_{K_4/K_5,\ K_6} \int_0^{[\mathrm{C_{tot}}]_\infty} (\mathrm{pH_{exp}} - \mathrm{pH_{sim}})^2 d[\mathrm{C_{tot}}], \quad \text{s.t. } [S_i] \geq 0\ \forall S_i \in \{\text{species in solution}\}, \tag{72}$$

was solved. The condition of positiveness of all concentrations makes sure the obtained solution is physically meaningful.

This is a nontrivial optimisation problem because it involves fitting the set of first-order differential equations (41–52) in $[C_{tot}]$ to the experimental pH data subjected to the algebraic constraint given by eq. (39), initial conditions given by eqs. (53–56) and matching the final conditions of pH_∞ and $[CO_2]_\infty$. The constrained, nonlinear least squares fitting of this set of differential-algebraic equations was formulated and solved in gPROMS version 4.1 (Process Systems Enterprise Ltd., UK; https://www.psenterprise.com/products/gproms) using gO:CAPE-OPEN to access the physical properties of the Aspen Plus database via the CAPE-OPEN interface standard [34–38].

External physical property packages are interfaced to gPROMS as Foreign Objects. Each distinct Physical Property Foreign Object used by a Model is declared as a Parameter of type `FOREIGN_OBJECT`. The latter keyword is normally followed by the class of the Foreign Object which identifies the external physical properties software that will be used to implement this instance of the Foreign Object. The standard way of referring to physical property calculations within the Model is as `ForeignObjectName.PhysicalProperty` for constant properties (mainly those relating to pure components properties such as molecular weights) and `ForeignObjectName.PhysicalProperty(`*InputList*`)` for variable physical properties. Each input of a physical property is a scalar or vector-valued variable or expression. Each property returns a single scalar or vector-valued quantity. The latter may be of type integer, logical or real. A method may be used anywhere in the Model where an expression of the corresponding dimensionality and type is allowed.

gPROMS comes as standard with the `COThermoFO` Foreign Object [39] which allows gPROMS models to make use of external thermodynamic and physical properties software that comply with version 1.1 of the CAPE-OPEN Thermodynamic and Physical Properties specification [40]. To do this, in the `PROCESS` entity the Foreign Object is declared to belong to class `COThermoFO`. Fig. 9 summarizes the major steps required to interface Aspen Plus with gPROMS.

What to do in Aspen Plus?

To use a physical property package from Aspen Plus in gPROMS a `*.cota` file must be created. The steps required in Aspen Properties or Aspen Plus are:

- Open or create a `*.bkp` file in Aspen Plus
- Specify the *components* (H_2O, CO_2, ...)
- Use the *Electrolyte Wizard* to generate ionic reactions and additional components that might be formed by the reactions (H_3O^+, OH^-, HCO_3^-, CO_3^{2-})
- Choose an appropriate *Property Method* (ELECNRTL: Electrolyte NRTL + Redlich-Kwong)
- Select Tools ⇒ Export CAPE-OPEN Package
- Save the `*.cota` file, e.g., `CO2-W-IL-sys.cota`, in the same folder as the gPROMS project file.

What to do in gPROMS?

The following steps are needed to incorporate a *.cota file in the gPROMS project file :

- In the `PARAMETER` section of the `MODEL` entity enter:
  PropPkgName `AS FOREIGN_OBJECT "COThermoFO"`
  where *PropPkgName* is the name by which the property package will be referred to in the `EQUATION` section
- In the `SET` section of `MODEL` or `PROCESS` entities enter:
  PropPkgName `:=`
  where *PropPkgFile* (see below) is the name of the *.cota file
- In the `EQUATION` section access properties via
  PropPkgName`.`*PropName*`(params)`

`"COThermoFO::(PS)ATCOProperties.COPropertySystem.1<`*PropPkgFile*`>";`

Model entity `Absorber` (Example of gPROMS `MODEL` entity)

```
PARAMETER
  PhysProps  AS FOREIGN_OBJECT "COThermoFO"  # external thermophysical property package
  COMPONENTS AS ORDERED_SET                  # set of components
  T          AS REAL                         # system temperature (K)
  P          AS REAL                         # system pressure    (K)

VARIABLE
  c    AS ARRAY(COMPONENTS) OF CONCENTRATION  # (mol/m^3)
  ctot AS CONCENTRATION                       # (mol/m^3)
  x    AS ARRAY(COMPONENTS) OF MOLE_FRAC      # (-)
  ac   AS ARRAY(COMPONENTS) OF ACTIVITY_COEFF # (-)

SET
  PhysProps := "COThermoFO::(PS)ATCOProperties.COPropertySystem.1<CO2-W-IL-sys>";

EQUATION
  ctot = SIGMA(c);  # total concentration
  x    = c/ctot  ;  # mole fractions
  ac = PhysProps.LiquidActivityCoefficient(T, P, x); # get values of activity coeffs
  '''
```

Figure 9. Summary of the workflow required for interfacing gPROMS and an Aspen Plus Property Package (interface direction: Aspen Plus → gPROMS) that complies with version 1.1 of the CAPE-OPEN Thermodynamic and Physical Properties specification.

Table 2. Equilibrium constants obtained from data fitting. For completeness, the values of all constants are listed, although only the ratio K_4/K_5 and K_6 were adjusted.

Equilibrium constant	Value
K_4	1.480×10^{13}
K_5/K_4	$\sim 10^{-5}$
K_6	264.1
K_7	6.957×10^{8}
K_8	187.9

Table 2 lists the equilibrium constants that best fit the experimental pH curve. The equilibrium constant K_6 was estimated with a small standard deviation (95% confidence interval equal to 0.42). However, the ratio K_5/K_4 is difficult to estimate with an equally small relative standard error. Despite this, the fitting results indicate that $K_5 \ll K_4$ and $[\mathrm{RH_2^{2+}}] \approx 0$; thus it is not possible to determine with certainty the value of K_5 because the reaction (5) has little impact on the results. It is thus concluded that the concentration of $\mathrm{RH_2^{2+}}$ in solution is ≈ 0, due to the high reactivity between the bicarbonate ion and the anion $[\mathrm{Lys^-}]$. Therefore, the second protonation occurs simultaneously with the bicarbonate binding to the amine of the side chain. Nevertheless, the simulated results show the existence of a small amount of $\mathrm{RH_2^{2+}}$ at the end of the experiment, when no more $\mathrm{CO_2}$ is absorbed, owing to the presence of some free amine groups in the medium.

Fig. 10 shows the simulated and fitted pH curves plotted against the $\mathrm{CO_2}$ loading concentration. The simulated pH curve is in excellent agreement with the experimental data. In particular, the model simulates quite nicely the smooth concave and convex curvatures of the experimental pH curve, which can be attributed to the protonation kinetics of the amines of $[\mathrm{Lys^-}]$.

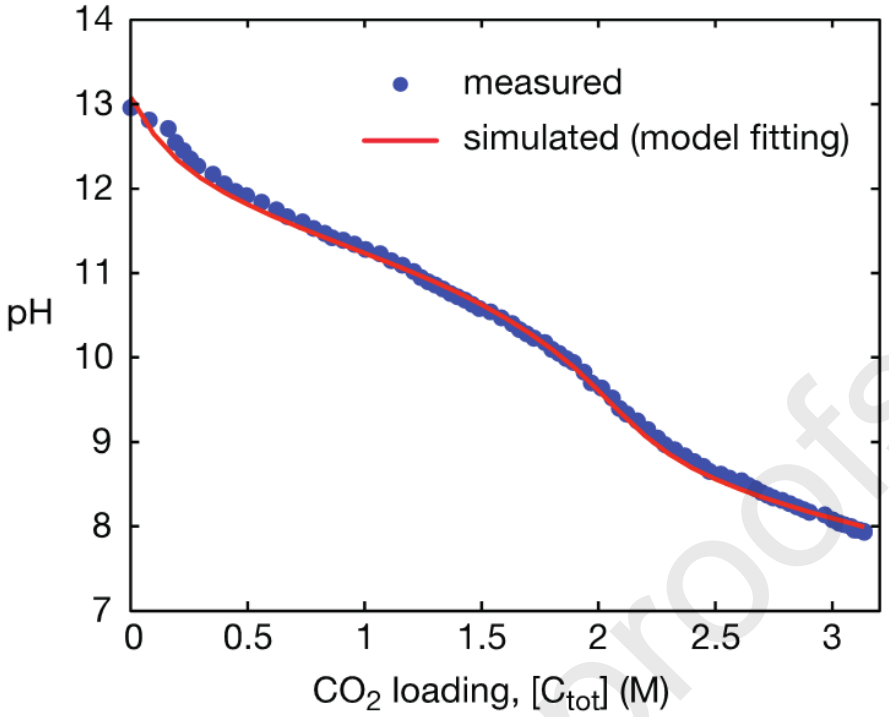

Figure 10. Experimental (symbols) and fitted (line) curves of pH as a function of CO_2 loading, $[C_{tot}]$ (M).

Since it is assumed that at each instant along the absorption experiment the concentrations of the various species in solution are governed by the corresponding chemical equilibrium constants then the overall absorption kinetics must be controlled by mass transfer from the gas to the liquid phase. Since the gaseous CO_2 flowing in the shell side of the contactor suffered a negligible pressure drop during the experiment (< 0.07 bar), it is safe to assume that the conditions prevailing in the shell side of the contactor were 1 atm and 20 °C, and what varied throughout the experiment was the volumetric (or molar) outlet flow rate of CO_2, $\dot{n}_{CO_2}^{(out)}$. Moreover, given that pure gas transport through the 0.65 μm pores of the Eclipse™ membrane filled with gas phase is a much faster process than bulk mixing and diffusion of the dissolved gas in the liquid-phase, the overall absorption kinetics should be controlled by mass transfer in the liquid phase. In thiscase, the overall differential material balance to the CO_2 can be written as

$$\frac{d(V[C_{tot}])}{dt} = k_L A_m([CO_2]_\infty - [CO_2]), \quad (73)$$

where A_{m} is the membrane contact area, k_{L} the mass transfer coefficient in the liquid phase, and, recall, $[\mathrm{CO_2}]_\infty$ the $\mathrm{CO_2}$ solubility in the aqueous solution of $[\mathrm{Cho^+}][\mathrm{Lys^-}]$ at 1 atm and 20 °C. This equation is more general than may seem at first glance. With reference to Fig. 5, the differential material balance to the $\mathrm{CO_2}$ can also be expressed as

$$\frac{d(V[\mathrm{C_{tot}}])}{dt} = Q\left([\mathrm{CO_2^L}]^{(\mathrm{out})} - [\mathrm{CO_2^L}]^{(\mathrm{in})}\right), \tag{74}$$

where $[\mathrm{CO_2^L}]^{(\mathrm{in})}$ and $[\mathrm{CO_2^L}]^{(\mathrm{out})}$ are the inlet and outlet concentrations of aqueous $\mathrm{CO_2}$ in the lumen (L) side of the membrane and Q the volumetric recirculation flow rate in that same side. Given that the aqueous IL solution is assumed to be well mixed, by definition $[\mathrm{CO_2^L}]^{(\mathrm{in})} = [\mathrm{CO_2}]$, where, as above, $[\mathrm{CO_2}]$ is the $\mathrm{CO_2}$ concentration in the bulk of volume V. Using a quasi-steady approximation, the differential material balance to the recirculating aqueous $\mathrm{CO_2}$ can be written as

$$Q\frac{d[\mathrm{CO_2^L}]}{dA_{\mathrm{m}}} = k_{\mathrm{L}}\left([\mathrm{CO_2}]_\infty - [\mathrm{CO_2^L}]\right), \tag{75}$$

Integrating this equation over the whole membrane area, A_{m}, over which $[\mathrm{CO_2^L}]$ changes from to $[\mathrm{CO_2^L}]^{(\mathrm{in})}$ to $[\mathrm{CO_2^L}]^{(\mathrm{out})}$, gives

$$\frac{[\mathrm{CO_2}]_\infty - [\mathrm{CO_2^L}]^{(\mathrm{in})}}{[\mathrm{CO_2}]_\infty - [\mathrm{CO_2^L}]^{(\mathrm{out})}} = \phi, \;\; \phi \equiv \exp\left(\frac{k_{\mathrm{L}}A_{\mathrm{m}}}{Q}\right), \tag{76}$$

and

$$[\mathrm{CO_2^L}]^{(\mathrm{out})} - [\mathrm{CO_2^L}]^{(\mathrm{in})} = \left(1 - \frac{1}{\phi}\right)\left([\mathrm{CO_2}]_\infty - [\mathrm{CO_2^L}]^{(\mathrm{in})}\right). \tag{77}$$

But since $[\mathrm{CO_2^L}]^{(\mathrm{in})} = [\mathrm{CO_2}]$, eq. (73) becomes

$$\frac{d(V[\mathrm{C_{tot}}])}{dt} = Q\left(1 - \frac{1}{\phi}\right)\left([\mathrm{CO_2}]_\infty - [\mathrm{CO_2}]\right), \tag{78}$$

which is the same as eq. (73) with $k_{\mathrm{L}}A_{\mathrm{m}}$ replaced by $Q(1-\phi^{-1})$. Moreover, $\lim_{Q\to\infty} Q(1-\phi^{-1}) = k_{\mathrm{L}}A_{\mathrm{m}}$. Thus, even if there is a concentration gradient along the extent of

the lumen side of the membrane, eq. (73) is still valid but with a slight change of the meaning of the product $k_L A_m$. The latter was determined by nonlinear least squares fitting of the experimental $[C_{tot}]$ curve as a function of time. This entailed solving the following optimisation problem:

$$\min_{k_L A_m} \int_0^{t_{end}} ([C_{tot}]_{exp} - [C_{tot}]_{sim})^2 dt, \tag{79}$$

where the subscripts $_{exp}$ and $_{sim}$ denote the experimental and simulated $[C_{tot}]$ curves and t_{end} the duration of the experiment. The estimated parameter value was $k_L A_m/V = 0.834\ \text{min}^{-1}$ (95% confidence interval of 2.3×10^{-6} and a standard deviation of 1.2×10^{-6}). Fig. 11 shows the simulated and fitted $[C_{tot}]$ curves plotted against process time. The simulated $[C_{tot}]$ curve is in excellent agreement with the experimental data.

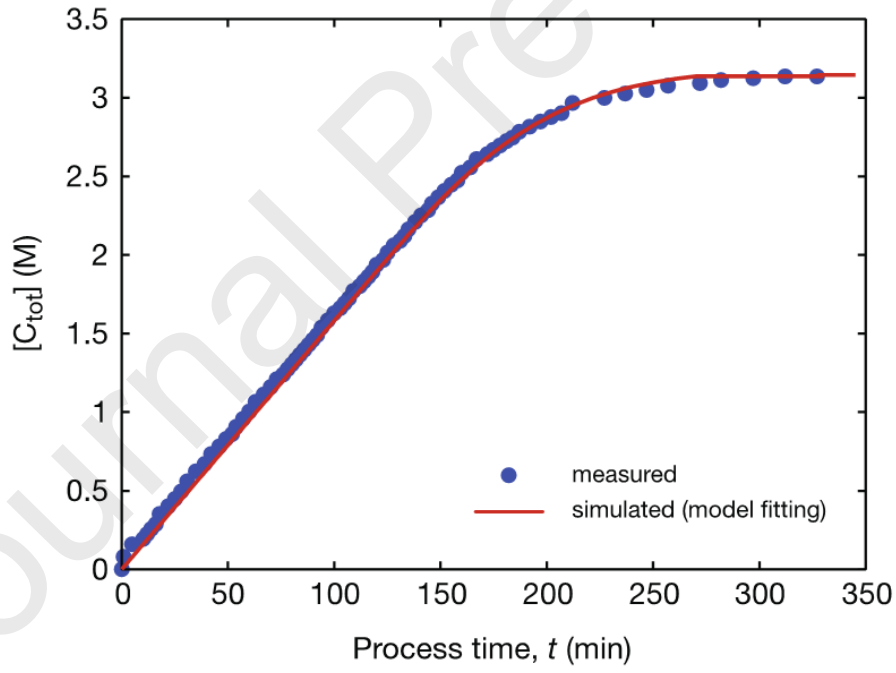

Figure 9. Experimental (symbols) and fitted (line) curves of CO_2 loading, $[C_{tot}]$ (M), as a function of process time.

Further simulated concentration profiles are plotted in Figs. 12–14. These are meant to illustrate the sort of quantitative information provided by the model. These profiles are not comparable with those published for the well-studied, traditional aqueous amine solutions.

Moreover, since there is no reported theoretical study in the literature on this system, it is not possible to make a comparison with data from other sources. Nevertheless, the good agreement between the simulated and experimental values, the likelihood of the trends displayed by the simulated concentration profiles, and reasonableness of the assumptions behind the chemical reaction equilibria support the validation of our model.

Fig. 12 shows the simulated $[\mathrm{Cho}^+][\mathrm{Lys}^-]$ concentration profile and its protonated forms as a function of the total CO_2 loading. The shape of the concentration profile for the single-protonated form is convex passing through a maximum and then tending towards progressively smaller values. This behaviour is consistent with the increase of P_1 concentration (Fig. 14), as a consequence of the bicarbonate ion attachment, evidenced in Fig. 13. As stated above, the concentration of R^{2+} is negligible throughout the experiment. The amount of free bicarbonate increases until it reaches a peak and then is progressively consumed until the end of the experiment when no more CO_2 is absorbed. The concentration profile of dissolved, unreacted CO_2 starts from near zero and increases monotonically towards the saturation value achieved with physical absorption, which is much smaller than the loading achieved by chemical absorption.

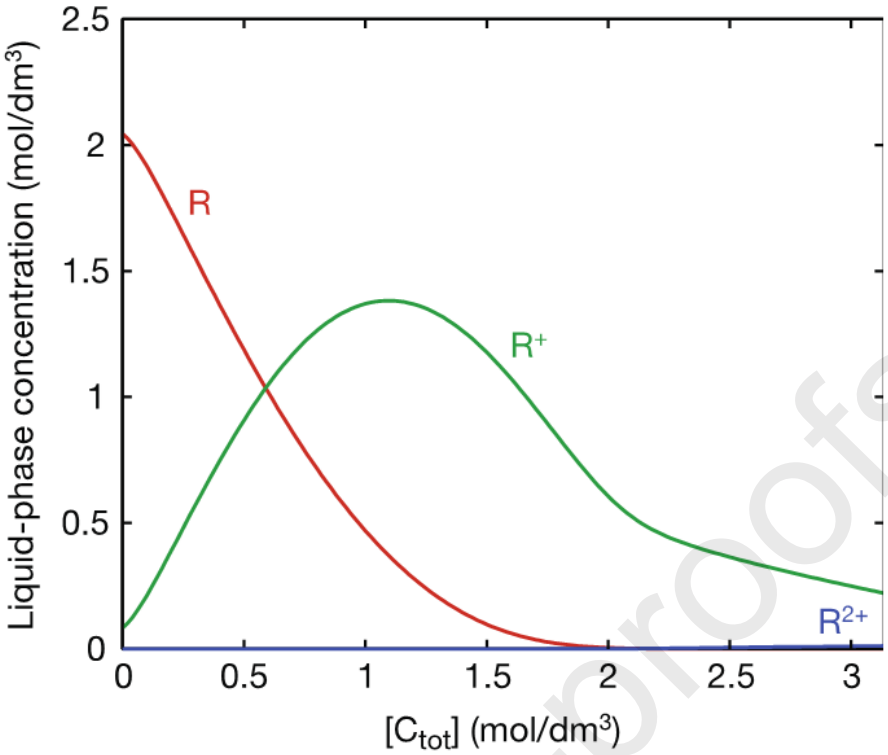

Figure 10. Simulated curves of $[R] \equiv [Cho^+][Lys^-]$ IL and its two positively charged forms, $[R^+] \equiv [Cho^+][Lys^{-+}]$ and $[R^{2+}] \equiv [Cho^+][Lys^{-++}]$, as a function of total CO_2 loading, $[C_{tot}]$.

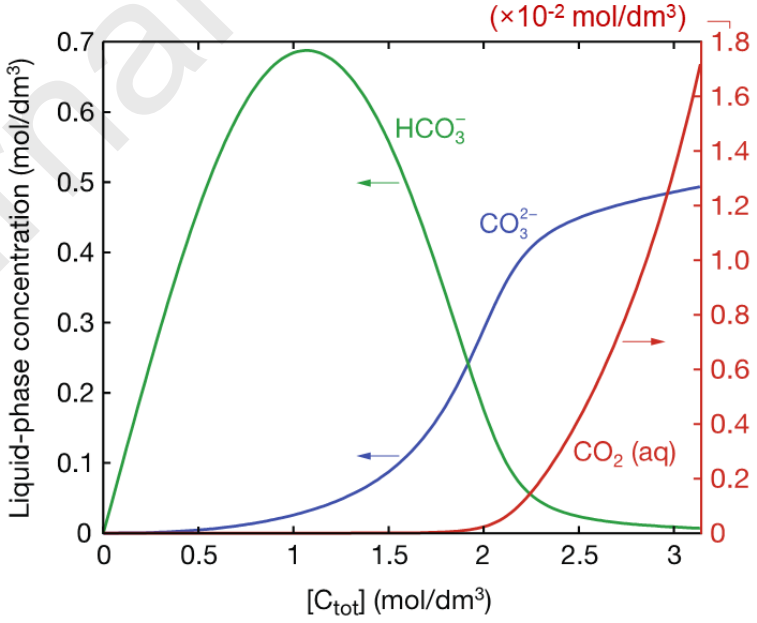

Figure 11. Simulated curves of $[CO_2\ (aq)]$, $[HCO_3^-]$, and $[CO_3^{2-}]$ as a function of total CO_2 loading, $[C_{tot}]$.

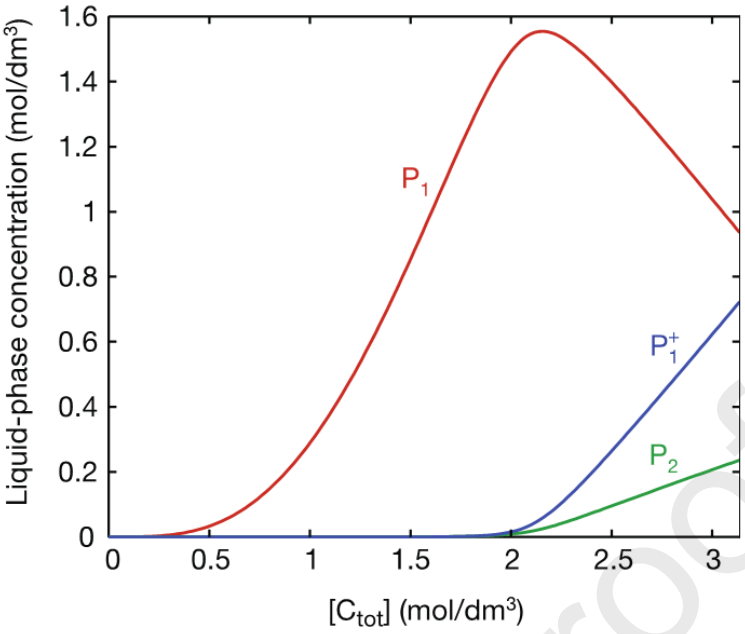

Figure 12. Simulated concentration curves of the final products, $P_1 \equiv [Cho^+][Lys^{-+}HCO_3^-]$ and $P_2 \equiv [Cho^+][Lys^{-++}2HCO_3^-]$, and intermediate species $P_1^+ \equiv [Cho^+][Lys^{-+}HCO_3^-]$ as a function of total CO_2 loading, $[C_{tot}]$.

Some recent works [41,42] have reported on the qualitative identification of amine, carbamate, and bicarbonate species during the absorption of CO_2 in aqueous solutions of various types of amines, but not in solutions of ILs with quaternary ammonium cations. Infrared monitoring allows quantitative measurements of multicomponent solutions provided the concentrations are within the range of validity of the Beer–Lambert law, but typically requires time-consuming calibration of pure components or mixtures at different concentrations [19,33,43].

Altought the experimental ATR-FTIR absorbance spectrum, A^{exp}, was measured as a function of CO_2 loading, $A^{exp} = A^{exp}([C_{tot}])$, it is in reality a multivariable function of the experimental species concentrations in solution, $[\underline{S} \in \mathcal{S}]^{exp}$, where $\mathcal{S} = \{H_2O, OH^-, ..., P_2\}$ represents the set of chemical species. Here we adopt a procedure somewhat similar to the calibration-free spectroscopic technique proposed by Richner and Puxty [20] for determining the speciation of CO_2–H_2O–alkanolamine systems. Their method is based on *in situ* infrared

monitoring of the liquid phase during CO_2 absorption by an aqueous amine solution in a stirred vessel, combined with mathematical hard modeling of the reaction mechanism. The species concentrations are calculated by fitting a thermodynamic model to multivariate spectroscopic measurements using nonlinear regression. In our procedure, however, the thermodynamic equilibrium constants of the CO_2–H_2O–$[Cho^+][Lys^-]$ system are those determined independently using our validated chemical reaction model, and the simulated profiles of species concentration as a function of CO_2 loading shown in Figs. 12–14, $[\underline{S}] = [\underline{S}]([C_{tot}]$, considered to be a good approximation of their experimental counterparts. This, in turn, allows us to replace the analysis of $A^{exp}([C_{tot}])$ by a multivariable analysis of $A^{exp}([\underline{S} \in \mathcal{S}])$, where $[\underline{S}] = [\underline{S}]([C_{tot}])$ is given by the thermodynamic model. It is shown next that $A^{exp}([\underline{S} \in \mathcal{S}])$ can be explained by a multivariable linear model and therefore the nonlinearities in A^{exp} $[C_{tot}]$ completely described by the thermodynamic model.

If the Beer–Lambert law is valid, the measured absorbance at any given wavenumber, say λ, in a multicomponent solution of $\mathcal{S}$ components can be expressed as

$$A_\lambda = \ell \sum_{S_i \in \mathcal{S}} \epsilon_{\lambda,i}[S_i] \,, \tag{80}$$

where ℓ is the path length, $[S_i]$ the molar concentration of species S_i, and $\epsilon_{\lambda,i}$ the molar attenuation coefficient (or molar absorptivity) of S_i at wavenumber λ. Despite the limitations of this law, in particulcar its failure to maintain a linear relationship between attenuation and concentration of analyte over the full range of concentration, here it is assumed that the change in the measured absorbance of the CO_2–water–$[Cho^+][Lys^-]$ solution at any given wavenumber, say λ, can be expressed as

$$dA_\lambda = \sum_{S_i \in \mathcal{S}} a_{\lambda,i} d[S_i] + de_\lambda \tag{81}$$

or, in integral form,

$$\Delta A_\lambda(t) = \sum_{S_i \epsilon \mathcal{S}} a_{\lambda,i} \Delta[S_i](t) + e_\lambda(t)\,, \tag{82}$$

where $\mathcal{S} = \{H_2O, OH^-, ..., P_2\}$ is the set of chemical species that make up the solution, $\Delta A_\lambda(t) = A_\lambda(t) - A_\lambda(0)$ and so forth, $a_{\lambda,i} \geq 0$ a nonnegative constant empirically related to the molar attenuation coefficient $\epsilon_{\lambda,i}$ and which for simplicity we shall refer to as an absorptivity coefficient, and $e_\lambda \sim \mathcal{N}(0,\sigma^2)$ a random residual or error assumed to be normally distributed with zero mean and standard deviation σ. In matrix notation,

$$\underline{A} = \boldsymbol{\Xi} \times [\underline{S}] + \underline{e}, \tag{83}$$

$$\begin{bmatrix} A_{\lambda_1} \\ \dots \\ A_{\lambda_m} \end{bmatrix} = \begin{bmatrix} \alpha_{\lambda_1,1} & \dots & \alpha_{\lambda_1,n} \\ \dots & & \dots \\ \alpha_{\lambda_m,1} & \dots & \alpha_{\lambda_m,n} \end{bmatrix} \begin{bmatrix} [S_1] \\ \vdots \\ [S_n] \end{bmatrix} + \begin{bmatrix} e_{\lambda_1} \\ \vdots \\ e_{\lambda_m} \end{bmatrix}, \tag{84}$$

where $\underline{A}$ is the m-vector of measured absorbances (*i.e.*, the absorbance spectrum), $\boldsymbol{\Xi}$ the $m \times n$ matrix of absorptivities, $[\underline{S}] = \left[[CO_2(aq)], [HCO_3^-], [R], ..., [P_2]\right]^T$ the n-vector of species concentrations, and $\underline{e}$ the m-vector of residual errors. The matrix $\boldsymbol{\Xi}$ can be determined by constrained multiple linear regression with a nonnegative least squares estimation technique:

$$\min_{\boldsymbol{\Xi}} \|\underline{e}\|^2 \text{ s.t. } \boldsymbol{\Xi} \geq 0 \tag{85}$$

(the elements of matrix $\boldsymbol{\Xi}$ must all be nonnegative). This parameter estimation problem was formulated and solved in gPROMS. To improve the robustness of the estimation, any absorptivity $a_{\lambda,i}$ whose $\sigma_{\lambda,i}/a_{\lambda,i}$ ratio is larger than five times the average value of $\sigma_{\lambda,i}/a_{\lambda,i}$ for each wavenumber λ, where $\sigma_{\lambda,i}$ is the standard deviation of the estimated value of $a_{\lambda,i}$, is discarded, and then the nonnegative linear regression is repeated but without the eliminated parameters. One iteration is enough to discard the absorptivities that contribute little to the objective function.

Table 3 summarises the obtained results and Fig. 16 compares the fitted and measured absorbances at the three selected wavenumbers plotted against the CO_2 loading concentration. The results clearly show that the chemical model and the corresponding fitted equilibrium constants are compatible with the ATR-FTIR data measured experimentally. The estimated values of $a_{\lambda,i}$

for HCO_3^- and CO_3^{2-} were either zero or their standard deviations very large and, therefore, discarded before further refitting. The estimated contribution of $CO_2(aq)$ to the measured ATR-FTIR signal is negligible because its concentration is very small in the aqueous IL solution. Also, the estimated value of $a_{\lambda,i}$ for RH_2^{2+} was either zero or very close to it. The standard deviations of the estimates of the remaining absorptivities are all small and, therefore, appear to contribute significantly to explain the experimental ATR-FTIR data.

Table 3: Values of the absorptivities for each component in the aqueous IL solution that best fit the experimental FTIR spectra. The 95% confidence interval of each estimated absorptivity is equal to 2σ.

λ (cm^{-1})	1647		1478		1358	
S_i	$a_{\lambda,i}$	$\sigma_{\lambda,i}/a_{\lambda,i}$	$a_{\lambda,i}$	$\sigma_{\lambda,i}/a_{\lambda,i}$	$a_{\lambda,i}$	$\sigma_{\lambda,i}/a_{\lambda,i}$
$CO_2(aq)$	00.0	*	0.000	*	00.0	*
HCO_3^-	00.0	**	0.000	*	00.0	**
CO_3^{2-}	00.0	*	0.000	**	00.0	*
R	70.7	0.004	0.509	0.004	90.6	0.008
RH^+	70.7	0.004	0.528	0.003	90.6	0.008
RH_2^{2+}	00.0	*	0.000	*	000.0	*
P_1	70.6	0.003	0.568	0.002	090.7	0.004
P_1^+	78.1	0.003	0.207	0.002	100.0	0.005
P_2	69.5	0.004	0.656	0.005	090.0	0.004

*Optimum value at lower bound. **Discarded.

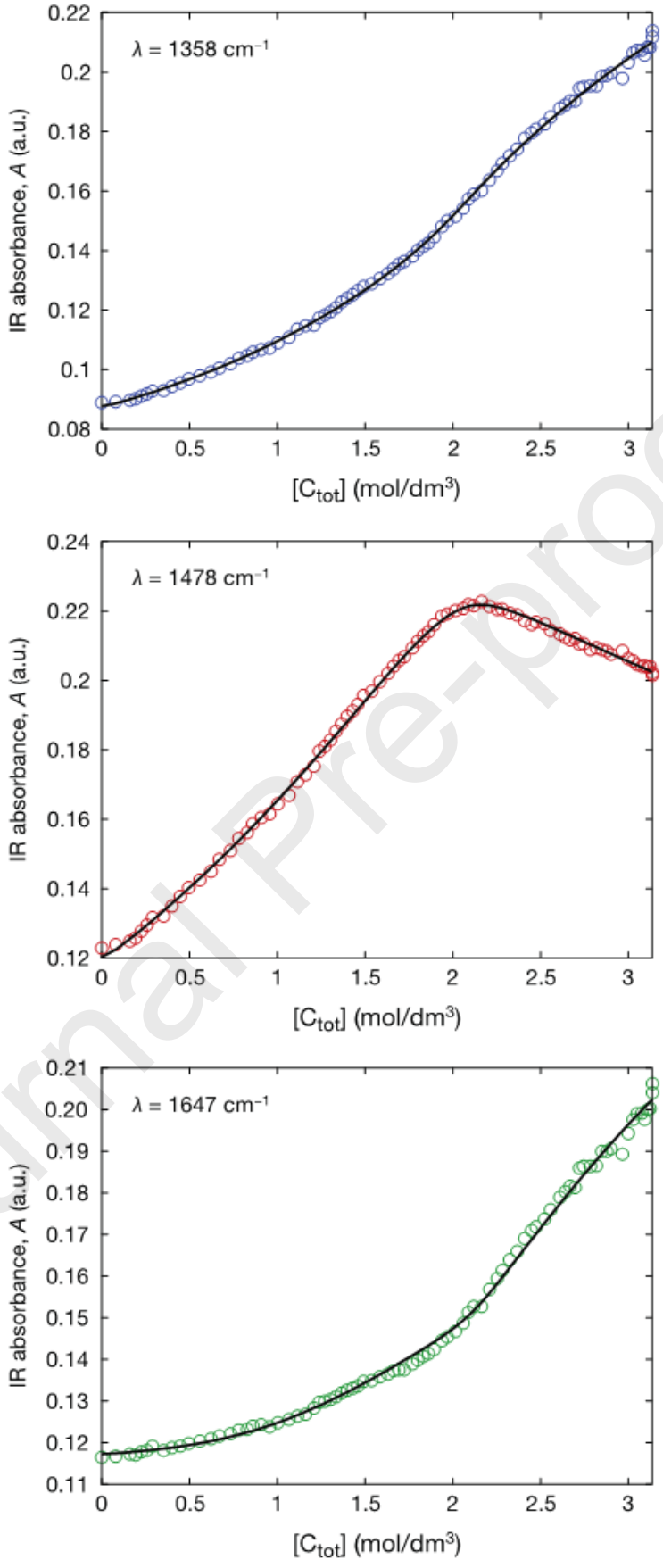

Figure 15. Experimental and simulated IR absorbances as function of CO_2 loading, [C_{tot}], at $1647\ cm^{-1}$, $1478\ cm^{-1}$, and $1358\ cm^{-1}$.

Interestingly, the proposed model is able to accurately fit the experimental ATR-FTIR absorbance profile as a function of CO_2 loading not only at the three selected wavenumbers, but also over the entire wavenumber range. This is demonstrated in Fig. 16, which compares the experimental and fitted ATR-FTIR absorbance spectra, $\Delta A_\lambda^{(exp)}$ and $\Delta A_\lambda^{(fit)}$, as a function CO_2 loading over the wavenumber range $1200 \leq \lambda \leq 1700\ cm^{-1}$. For a better assessment of the quality of the fitting, the absorbance difference, $\Delta A_\lambda^{(fit)} - \Delta A_\lambda^{(exp)}$, is also plotted. Notice that absorbance scale of the 3D plots of $\Delta A_\lambda^{(exp)}$ and $\Delta A_\lambda^{(fit)}$ is $0 \leq \Delta A \leq 0.12$ a.u., whereas that of $\Delta A_\lambda^{(fit)} - \Delta A_\lambda^{(exp)}$ is 15 times smaller: $0 \leq \Delta\Delta A_\lambda \leq 0.008$ a.u.

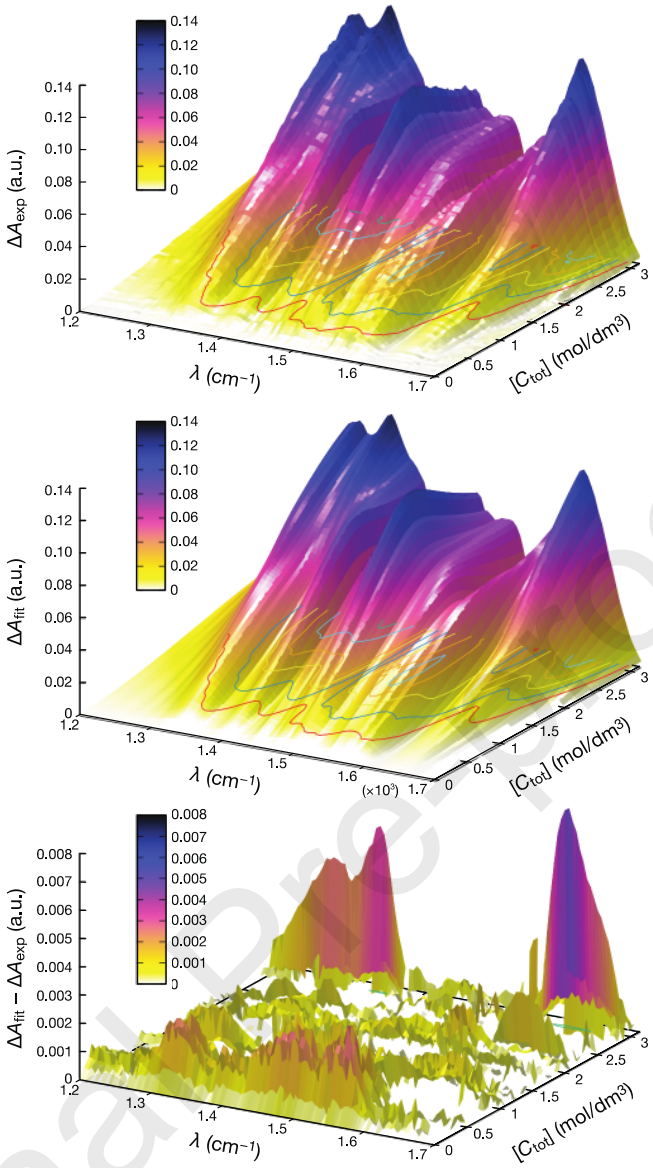

Figure 16: Comparison of the experimental and fitted ATR-FTIR absorbance spectra, $\Delta A_\lambda^{(\mathrm{exp})}$ and $\Delta A_\lambda^{(\mathrm{fit})}$, and their difference, $\Delta A_\lambda^{(\mathrm{fit})} - \Delta A_\lambda^{(\mathrm{exp})}$, as a function $\mathrm{CO_2}$ loading over the wavenumber range $1200 \leq \lambda \leq 1700\ \mathrm{cm}^{-1}$.

It can be argued that the excellent fitting of the ATR-FTIR absorbance profile $\Delta A_\lambda([C_{\mathrm{tot}}])$ for each fixed wavenumber λ is the result of a somewhat large number of fitting parameters: the five $a_{\lambda,i}$ for $i \in \{\mathrm{R},\mathrm{RH}^+,\mathrm{P_1},\mathrm{P_1^+},\mathrm{P_2}\}$. However, Fig. 17 shows that this is not the case. The plots in Fig. 17 of the five $a_{\lambda,i}$'s as a function of wavenumber over the range $1200 \leq \lambda \leq 1700\ \mathrm{cm}^{-1}$ show that, for all purposes, the experimental ATR-FTIR absorbance profile as a function $\mathrm{CO_2}$

loading can be explained by the multivariate linear regression of just three concentrations: $[P_1^+]$, $[P_2]$, and the aggregate concentration $[R] + [RH^+] + [P_1]$. Fig. 17 also shows the regions of the spectrum where the absorbance is less sensitive to changes in the composition and molecular structure of the solution. The values of $a_{\lambda,i}$ are significantly smaller over the wavenumber region $1390 \leq \lambda \leq 1570\ \mathrm{cm}^{-1}$ (except for a small peak centered at $1511\ \mathrm{cm}^{-1}$) than elsewhere in the explored domain $1200 \leq \lambda \leq 1700\ \mathrm{cm}^{-1}$, implying that for $1390 \leq \lambda \leq 1570\ \mathrm{cm}^{-1}$ the absorbance is less sensitive to changes in the composition and concentration of the aqueous IL solution.

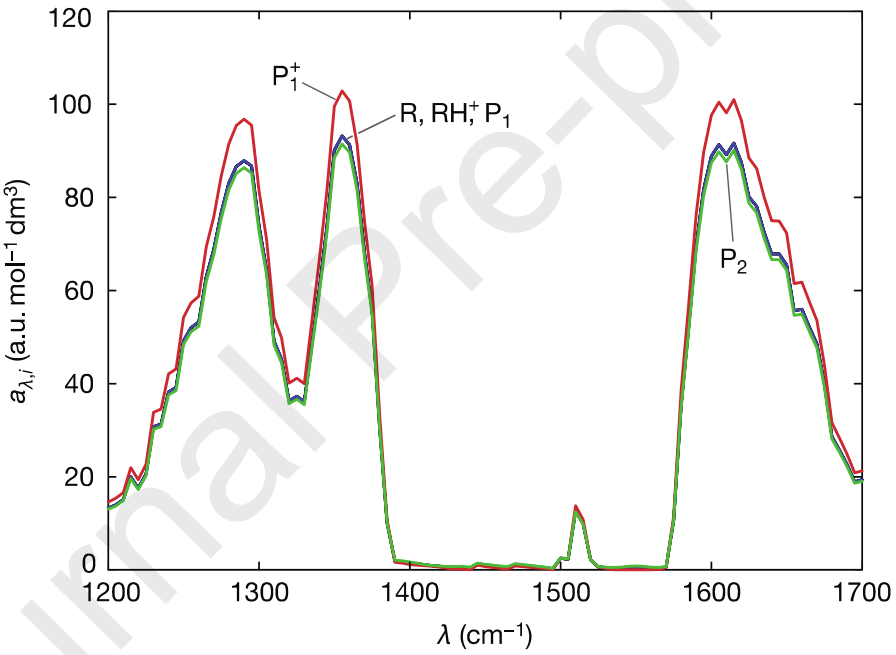

Figure 17: Plots of the five fitting parameters $a_{\lambda,i}$, $i \in \{R, RH^+, P_1, P_1^+, P_2\}$, as a function of the wavenumber over the range $1200 \leq \lambda \leq 1700\ \mathrm{cm}^{-1}$. For all purposes, the curves of $a_{\lambda,R}$, a_{λ,RH^+}, and a_{λ,P_1} are superposed.

Overall, the proposed model and solution procedure to explain the chemical absorption mechanism using the pH and ATR-FTIR data appear to be robust. On the one hand, the model provides not only the equilibrium constants of the reversible reactions of protonation of the amine

groups and bicarbonate binding, concentration profiles of the compounds involved in the reactions for the CO_2–$[Cho^+][Lys^-]$–water system, and overall mass-transfer coefficient based on liquid-phase concentrations, but also a better understanding of the chemical absorption mechanism. On the other hand, the model is also the basis for a chemometric analysis of the experimental ATR-FTIR data and the proposed procedure corroborates the possibility of using ATR-FTIR analysis for CO_2 monitoring in this complex aqueous medium. In addition, the method is applicable to a wide range of CO_2 loadings, since it combines the sensitivity of two different analytical methods.

5. Conclusions

We have performed experiments of CO_2 capture into a 50 wt% $[Cho^+][Lys^-]$ IL solution up to saturation conditions, using a PTFE membrane contactor to promote the contact between the gas and liquid phases. The absorption mechanism of CO_2 in the aqueous $[Cho^+][Lys^-]$ solution was investigated, and a chemical model was proposed for the CO_2–$[Cho^+][Lys^-]$–water system. The unknown chemical equilibrium constants—those of the reversible reactions of amine groups protonation and bicarbonate binding—were determined by fitting the experimental pH curve as a function of CO_2 loading. The validated model provides, among other information, the equilibrium constants of the reversible reactions of protonation of the amine groups and bicarbonate binding, concentration profiles of the compounds involved in the reactions for the CO_2–$[Cho^+][Lys^-]$–water system as function of CO_2 loading, and overall mass-transfer coefficient based on liquid-phase concentrations. From the analysis of the ATR-FTIR spectra, we identified peaks and observed changes in their absorbances with CO_2 loading. The variations observed in the entire FTIR spectrum are due to the increased concentration of IR absorbing ionic moieties in the aqueous IL medium; in particular, it is shown that the changes in the ATR-FTIR spectra with CO_2

loading can be explained by the multivariate linear regression of just three concentrations: $[P_1^+]$, $[P_2]$, and the aggregate concentration $[R] + [RH^+] + [P_1]$. The results presented in this study corroborate the potential of using ATR-FTIR as a tool for monitoring CO_2 absorption in this complex aqueous medium.

Acknowledgements

This work was supported by the **Associate Laboratory for Green Chemistry - LAQV** which is financed by national funds from FCT/MCTES (**UIDB/50006/2020**). C. F. Martins acknowledges Fundação para a Ciência e Tecnologia (FCT) for the fellowship SFRH/BD/111128/2015. Luísa A. Neves acknowledges FCT for her exploratory project grant IF/00505/2014/CP1224/CT0004 attributed within the 2014 FCT research program. Ricardo Chagas acknowledges FCT and FCT/MTES through the project grant UID/CTM/50025/2019.

References

[1] C.R. Stabernack, R. Brown, M.J. Laster, R. Dudziak, E.I. Eger, Absorbents differ enormously in their capacity to produce compound A and carbon monoxide, Anesth. Analg. 90 (2000) 1428–1435.

[2] D.M. Muñoz, A.F. Portugal, A.E. Lozano, J.G. De La Campa, J. De Abajo, New liquid absorbents for the removal of CO_2 from gas mixtures, Energy Environ. Sci. 2 (2009) 883–891.

[3] J. Wilcox, Carbon Capture, 1st ed., Springer-Verlag, New York, 2012.

[4] P. Styring, E. Quadrelli, K. Armstrong, Carbon dioxide utilisation: closing the carbon cycle., Elsevier, 2015.

[5] A.M. Pinto, H. Rodríguez, A. Arce, A. Soto, Combined physical and chemical absorption of carbon dioxide in a mixture of ionic liquids, J. Chem. Thermodyn. 77 (2013) 197–205.

[6] J.M. Gomes, S.S. Silva, R.L. Reis, Biocompatible ionic liquids: Fundamental behaviours and applications, Chem. Soc. Rev. 48 (2019) 4317–4335. doi:10.1039/c9cs00016j.

[7] C.F. Martins, L.A. Neves, M. Estevão, A. Rosatella, V.D. Alves, C.A.M. Afonso, J.G. Crespo, I.M. Coelhoso, Effect of water activity on carbon dioxide transport in cholinium-based ionic liquids with carbonic anhydrase, Sep. Purif. Technol. 168 (2016) 74–82.

[8] S. Yuan, Y. Chen, X. Ji, Z. Yang, X. Lu, Experimental study of CO_2 absorption in aqueous cholinium-based ionic liquids, Fluid Phase Equilib. 445 (2017) 14–24.

[9] S. Yuan, Z. Yang, X. Ji, Y. Chen, Y. Sun, X. Lu, CO_2 Absorption in Mixed Aqueous Solution of MDEA and Cholinium Glycinate, Energy and Fuels. 31 (2017) 7325–7333.

[10] X.D. Hou, Q.P. Liu, T.J. Smith, N. Li, M.H. Zong, Evaluation of Toxicity and

Biodegradability of Cholinium Amino Acids Ionic Liquids, PLoS One. 8 (2013).

[11] K. Simons, W.D.W.F. Brilman, H. Mengers, K. Nijmeijer, M. Wessling, Kinetics of CO_2 Absorption in Aqueous Sarcosine Salt Solutions : Influence of Concentration , Temperature , and CO_2 Loading, Ind. Eng. Chem. Res. 49 (2010) 9693–9702.

[12] P.S. Kumar, J.A. Hogendoorn, P.H.M. Feron, G.F. Versteeg, New absorption liquids for the removal of CO_2 from dilute gas streams using membrane contactors, Chem. Eng. Sci. 57 (2002) 1639–1651.

[13] A.F. Portugal, P.W.J. Derks, G.F. Versteeg, F.D. Magalhães, A. Mendes, Characterization of potassium glycinate for carbon dioxide absorption purposes, Chem. Eng. Sci. 62 (2007) 6534–6547.

[14] Y. Sistla, A. Khanna, CO2 absorption studies in amino acid-anion based ionic liquids, Chem. Eng. J. 273 (2015) 268–276.

[15] X. Zhou, G. Jing, F. Liu, B. Lv, Z. Zhou, Mechanism and Kinetics of CO_2 Absorption into an Aqueous Solution of a Triamino-Functionalized Ionic Liquid, Energy and Fuels. 31 (2017) 1793–1802.

[16] H. Guo, Z. Zhou, G. Jing, Kinetics of carbon dioxide absorption into aqueous [Hmim][Gly] solution, Int. J. Greenh. Gas Control. 16 (2013) 197–205.

[17] B. Lv, G. Jing, Y. Qian, Z. Zhou, An efficient absorbent of amine-based amino acid-functionalized ionic liquids for CO_2 capture: High capacity and regeneration ability, Chem. Eng. J. 289 (2016) 212–218.

[18] H. Suleman, A.S. Maulud, A. Syalsabila, M.Z. Shahid, The contribution of aqueous L-arginine salts to equilibrium carbon dioxide absorption in a co-promoter role at high pressure, Fluid Phase Equilib. 524 (2020) 112743.

[19] B.H. Stuart, Infrared Spectroscopy: Fundamentals and Applications B, John Wiley & Sons, Ltd, 2004.

[20] G. Richner, G. Puxty, Assessing the chemical speciation during CO_2 absorption by aqueous amines using in situ FTIR, Ind. Eng. Chem. Res. 51 (2012) 14317–14324.

[21] J. Sun, N.V.S.N.M. Konda, J. Shi, R. Parthasarathi, T. Dutta, F. Xu, C.D. Scown, A. Simmons, S. Singh, CO_2 enabled process integration for the production of cellulosic ethanol using bionic liquids, Energy Environ. Sci. 9 (2016) 2822–2834.

[22] J.L. McDonald, R.E. Sykora, P. Hixon, A. Mirjafari, J.H. Davis, Impact of water on CO_2 capture by amino acid ionic liquids, Environ. Chem. Lett. 12 (2014) 201–208.

[23] P. Prakash, A. Venkatnathan, Site-Specific Interactions in CO_2 Capture by Lysinate Anion and Role of Water Using Density Functional Theory, J. Phys. Chem. C. 122 (2018) 12647–12656.

[24] David R Lide, CRC Handbook of Chemistry and Physics, 84th Edition, 2003-2004, Handb. Chem. Phys. (2003).

[25] C.-C. Chen, H.I. Britt, J.F. Boston, L.B. Evans, Local Composition Model for Excess Gibbs Energy of Electrolyte Systems, AlChe J. 28 (1982) 588–596.

[26] C. -C Chen, L.B. Evans, A local composition model for the excess Gibbs energy of aqueous electrolyte systems, AIChE J. 32 (1986) 444–454.

[27] C.C. Chen, Y. Song, Generalized electrolyte-NRTL model for mixed-solvent electrolyte systems, AIChE J. 50 (2004) 1928–1941.

[28] O. Redlich, J.N.S. Kwong, On the Thermodynamics of Solutions., Chem. Rev. 44 (1949) 233–244.

[29] K.S. Pitzer, Electrolytes. From Dilute Solutions to Fused Salts, J. Am. Chem. Soc. 102 (1980) 2902–2906.

[30] R.M. Felder, R.W. Rousseau, L.G. Bullard, Felder's Elementary Principles of Chemical Processes, 4th ed., Wiley, New York, 2016.

[31] C.F. Martins, L.A. Neves, R. Chagas, L.M. Ferreira, C.A.M. Afonso, J.G. Crespo, I.M. Coelhoso, CO_2 removal from anaesthesia circuits using gas-ionic liquid membrane contactors, Sep. Purif. Technol. In press, (2020) 116983.

[32] M.M. Villar-Chavero, J.C. Domínguez, M.V. Alonso, V. Rigual, M. Oliet, F. Rodriguez, Viscoelastic properties of physical cellulosic bionogels of cholinium lysinate, Int. J. Biol. Macromol. 133 (2019) 262–269.

[33] A. Archane, W. Fürst, E. Provost, Influence of poly(ethylene oxide) 400 (PEG400) on the absorption of CO_2 in diethanolamine (DEA)/H_2O systems, J. Chem. Eng. Data. 56 (2011) 1852–1856.

[34] J.P. Belaud, M. Pons, Open software architecture for process simulation: The current status of CAPE-OPEN standard, Comput. Aided Chem. Eng. 10 (2002) 847–852.

[35] M. Pons, The CAPE-OPEN interface specification for reactions package, Comput. Aided Chem. Eng. 14 (2003) 863–868.

[36] J. van Baten, R. Szczepanski, A thermodynamic equilibrium reactor model as a CAPE-OPEN unit operation, Comput. Chem. Eng. 35 (2011) 1251–1256.

[37] J. Van Baten, M. Pons, Cape-open: Interoperability in industrial flowsheet simulation software, Chemie-Ingenieur-Technik. 86 (2014) 1052–1064.

[38] G. Tolksdorf, E. Esche, J. van Baten, G. Wozny, Taylor-Made Modeling and Solution of Novel Process Units by Modular CAPE-OPEN-based Flowsheeting, Comput. Aided Chem. Eng. 38 (2016) 787–792.

[39] gROMS Physical Properties Guide, Release v3.7. (2013) Process Systems Enterprise Ltd. http://www.psenterprise.com.

[40] CO-LaN Consortium, Thermodynamic and Physical Properties version 1.1, ver. 3.11, CAPE-OPEN Laboratories Network, (2011).

[41] P. Jackson, K. Robinson, G. Puxty, M. Attalla, In situ Fourier Transform-Infrared (FT-IR) analysis of carbon dioxide absorption and desorption in amine solutions, Energy Procedia. 1 (2009) 985–994.

[42] K. Robinson, A. Mccluskey, M.I. Attalla, An FTIR Spectroscopic Study on the Effect of Molecular Structural Variations on the CO_2 Absorption Characteristics of Heterocyclic Amines, ChemPhysChem. 12 (2011) 1088–1099.

[43] P.W.J. Derks, P.J.G. Huttenhuis, C. Van Aken, J.H. Marsman, G.F. Versteeg, Determination of the liquid-phase speciation in the MDEA-H_2O-CO_2 system, Energy Procedia. 4 (2011) 599–605.

Highlights

- CO_2 absorption in aqueous $[Cho^+][Lys^-]$ IL is studied via mechanistic modelling
- A model of chemisorption and absorption dynamics is proposed and validated
- The constants of protonation reactions and bicarbonate binding are determined
- The overall mass-transfer coefficient on the liquid-phase side is determined
- The potential use of ATR-FTIR as monitoring tool of CO_2 absorption is demonstrated